Physics and Applications of Resonant Tunneling Devices

Thesis by

Sidney Chunping Kan

In Partial Fulfillment of the Requirements

for the Degree of

Doctor of Philosophy

California Institute of Technology

Pasadena, California

1991

(Defended May 23, 1991)

To my parent, my brother and Gladys

Acknowledgments

The Caltech years gave me joys and excitement as well as frustration and disappointments which I couldn't imagine before I came to Caltech. All these emotions were shared with a group of extraordinary people whom I would like to acknowledge again before I quit Caltech. The first great guy I want to acknowledge is my advisor, Professor Amnon Yariv. I am so thankful to him for his advice on my graduate study, the chance he gave me to work on the world's most powerful epitaxial growth system, the Molecular Beam Epitaxy (MBE) system and the chance to work with a team of intelligent colleagues. The second Cal-Techer I would like to thank particularly is Dr. Pamela Derry. She taught me all the basics about the MBE system and the GaAs processing techniques. I would also like to thank Dr. Norman Kwong who taught me about real research life, Professor Hadis Morkoç who taught me the advanced techniques of MBE, and Dr. Haila Wang who taught me the advanced GaAs processing techniques.

I am also thankful to Professor Tien-Ron Chen, Dr. Joel Paslaski, Dr. Michael Mittelstein, Ya-Yun Liu, Yu-Hua Zhuang Dr. Howard Chen, Ali Grafferi, Dr. Hal Zarem, Desmond Armstrong, Jana Mercado, Dr. David Mehuys, and more recently, Gladys Lang, Shu-Wu Wu, Ilan Grave, Dr. Giora Griffel, Steve Sanders, Lars Eng, Naohiro Kuze, Dr. Ron Agranat, William Marshall, Victor Leyva, Dr. Amir Sa'ar, Bin Zhou, Yuan-Jian Xu, John Iannelli, Kelvin Cooper, Chuck Neugebauer, and Thomas Schrans for their help.

I would also like to acknowledge the support from San Diego Supercomputer Center for the CRAY time and Dr. Mingchung Chu who introduced me to the basics of CRAY.

Finally, I thank Ruth Stratton for proofreading the original manuscript.

Abstract

This thesis addresses several important issues of the physics and applications of double barrier resonant tunneling devices on which the author worked during his graduate study at Caltech:

(1) Epitaxial growth of AlAs/GaAs double barrier resonant tunneling structure on both GaAs and Si substrate (Chapter 2).

(2) Investigation of terahertz modulation of resonant tunneling effect (Chapter 3).

(3) Study of the imaginary potential in double barrier resonant tunneling (Chapter 4).

(4) Development of the first series of optical resonant tunneling devices and parallel resonant tunneling (Chapter 5).

The history of the development of double barrier resonant tunneling and the basic theory are also discussed (Chapter 1).

Abbreviations

DBRT	Double Barrier Resonant Tunneling
MBE	Molecular Beam Epitaxy
OPT	Optically-controlled Parallel resonant-Tunneling
RTL	Resonant Tunneling Laser
I-V	Current-Voltage

Author's Publications Related to This Thesis

[1] S. C. Kan, H. Morkoç, A. Yariv, "GaAs/AlAs Double-Barrier Resonant Tunneling Structure on Si with Large Peak to Valley Ratio at Room Temperature," Applied Physics Letters, Vol. 52, 2250-2251 (1988).

[2] S. Kalem, J. Chyi, C. W. Litton, H. Morkoç, S. C. Kan and A. Yariv, "Electrical Properties of InAs Epilayers Grown by Molecular Beam Epitaxy on Si Substrates," Applied Physics Letters, Vol. 53, 562-564 (1988).

[3] S. C. Kan and A. Yariv, "The Ultimate Frequency Response and Time Evolution of Resonant Tunneling in Double-Barrier Structures," Journal of Applied Physics, Vol. 64, 3098-3105 (1988).

[4] S. C. Kan and A. Yariv, "Lifetime of the Quasi-Bound State in the Quantum Well in a Double-Barrier Structure with a Localized Imaginary Potential," Journal of Applied Physics, Vol. 67, 1957-1961 (1990).

[5] A. Sa'ar, S. C. Kan and A. Yariv, "Incoherent Resonant Tunneling without Reflection in Asymmetric Double-Barrier Structures," Journal of Applied Physics, Vol. 67, 3892-3894 (1990).

[6] I. Grave', S. C. Kan, G. Griffel, S. Wu, A. Sa'ar and A. Yariv, "A Monolithic Integration of a Resonant Tunneling Diode and a Quantum Well Semiconductor Laser," 1990 Conference on Lasers and Electro-Optics (CLEO), 21-25 May, Anaheim, California, Paper CPDP28.

[7] I. Grave', S. C. Kan, G. Griffel, S. Wu, A. Sa'ar and A. Yariv, "Integrated Double Barrier Resonant Tunneling Quantum Well Laser," Applied Physics Letters, Vol. 58, 110-112 (1991).

[8] S. C. Kan, S. Wu, S. Sanders, G. Griffel and A. Yariv, "Negative Photoconductivity in Double-Barrier Resonant Tunneling Diode," Annual Meeting of Optical Society of America, 4-9 November, 1990, Paper TuA2.

[9] S. C. Kan, S. Wu, S. Sanders, G. Griffel and A. Yariv, "Optically Controlled Resonant Tunneling in a Double-Barrier Diode," Journal of Applied Physics, Vol. 69, 3384, 1991.

[10] S. C. Kan, S. Sanders, G. Griffel, G. H. Lang, S. Wu and A. Yariv, "Optical Switching of a New Middle Trace in an Optically-controlled Parallel resonant-Tunneling device - Observation and Modeling," Applied Physics Letters, Vol. 58, 1548, 1991.

Table of Contents

Chapter One

Introduction to DBRT

Chapter One

Introduction to DBRT

The double barrier resonant tunneling (DBRT) effect was first proposed and demonstrated by Tsu, Chang and Esaki in 1973 [1-2]. It became an active research area in recent years after a demonstration of a very fast response (2.5 THz) by Sollner et al. in 1983 [3] . In this chapter, the basic principle of DBRT will be introduced and the development of DBRT will be discussed.

1.1 Basic Principle of DBRT

A typical DBRT device and its potential profile are shown in fig. 1.1. It is a two-terminal device which consists of a double barrier structure sandwiched between the emitter electrode and collector electrode. A typical I-V curve of this device is shown in fig. 1.2. The I-V curve consists of a sharp peak due to resonant tunneling effect which is explained as follows.

Because of the small size (about 50Å) of the quantum well between the two barriers, several discrete energy levels exist inside the quantum well. When a voltage V_a is applied across the double barrier structure as shown in fig. 1.2, the Fermi level of the emitter electrode is raised relative to the ground level in the quantum well. If the Fermi level is lower than the ground level in the quantum well as shown in fig. 1.3a, most of the electrons at the emitter electrode do not have enough energy to tunnel

through the ground level. The tunneling current is then very small. When V_a is increased so that the Fermi level becomes closer to the ground level, more electrons have enough energy to reach the ground level. Then the tunneling current increases as shown in fig. 1.3b. When the applied voltage is further increased so that the Fermi level is above the ground level, the electrons cannot tunnel through the ground state and the tunneling current then decreases as shown in fig. 1.3c. This leads to a sharp peak in the I-V curve shown in fig. 1.2. Multiple peaks in the I-V curve can also be observed if there are several discrete levels inside the quantum well. However, in a typical DBRT structure which is designed to produce a large resonance peak associated with the ground state, only one to two discrete states exist inside the quantum well.

In the following, we will derive an expression for the tunneling current based on the theory given by Tsu, Chang and Esaki [1-2]. We first define: (i) J_{left} as the sum of the particle currents incident on the double barrier structure from the electrode on the left (emitter) and (ii) J_{right} as the sum of the particle currents from the electrode on the right (collector). The total current J_{total} is equal to the difference, $J_{left} - J_{right}$. In order to calculate J_{left} and J_{right} , we have to calculate the particle current, $J(k_1)$, due to a single particle, where k_1 is the z-component of the incident wavevector of the particle wavefunction and the z-direction is normal to the barrier layers.

We first calculate the eigenfunctions of the DBRT structure by solving the Schrödinger Equation. Each eigenfunction describes a particle incident

from one side of the structure, reflected back and transmitted to another side as shown in fig. 1.4. The particle current density, $J(k_1)$, is given by:

$$J(k_1) = \frac{e\,\hbar}{2m^*i}\left(\psi^*_{k_1}\frac{\partial}{\partial z}\psi_{k_1} - \psi_{k_1}\frac{\partial}{\partial z}\psi^*_{k_1} \right) \tag{1.1}$$

where e is the electronic charge, $\hbar = h/2\pi$ and h is Planck's constant, m^* is the effective mass of the electron in the layer material which is different from layer to layer, Ψ_{k_1} is the eigenfunction:

$$\Psi_{k_1} = \begin{cases} \exp(ik_1z) + a_{12}\exp(-ik_1z) & \text{in layer I} \\ a_{21}\exp(ik_2z) + a_{22}\exp(-ik_2z) & \text{in layer II} \\ a_{31}\exp(ik_3z) + a_{32}\exp(-ik_3z) & \text{in layer III} \\ a_{41}\exp(ik_4z) + a_{42}\exp(-ik_4z) & \text{in layer IV} \\ a_{51}\exp(ik_5z) & \text{in layer V} \end{cases}$$

The coefficients, a_{ij}, can be found by matching Ψ_{k_1} and $\nabla\Psi_{k_1}/m^*$ at each interface, k_i, $(2 \le i \le 5)$, are the z-component of the wavevector at different layers which depend on k_1 . The particle current $J(k_1)$ calculated by equation (1.1) using the wavefunction in layer V is given by:

$$J(k_1) = e\,|a_{51}|^2\,\hbar k_5/m^*$$

The transmission coefficient $|a_{51}|^2$ versus the longitudinal energy, $(\hbar k_1)^2/2m^*$, is plotted in fig. 1.5. The peak in fig. 1.5 shows that only those electrons within a narrow range of k_1 can possess a significantly large tunneling amplitude. The states with large tunneling amplitude are the discrete levels of the quantum well.

To obtain an expression for J_{left} , we sum up $J(k_1)$ with different weighting factors according to the Fermi-Dirac distribution:

$$J_{left}=\int \frac{d^3\vec{k}}{(2\pi)^3}\ 2\ f(\vec{k})\ J(k_1)$$

where $\vec{k} = (k_x, k_y, k_1)$, $f(\vec{k})$ is the Fermi-Dirac distribution of layer I, and the factor of two is due to the spin degeneracy. Since $J(k_1)$ depends on k_1 only, we can integrate the expression over the transverse components, k_x and k_y . J_{right} is calculated in a similar way. Finally, we take the difference, $J_{left} - J_{right}$, to obtain the expression for J_{total} :

$$J_{total} = \frac{em^*kT}{2\pi^2\hbar^3}\int_0^\infty |a_{51}|^2\frac{k_5}{k_1} \times \log\left(\frac{1+\exp[(E_f - E_z)/kT]}{1+\exp[(E_f - E_z - eV_a)/kT]}\right) dE_z \qquad (1.2)$$

where k is Boltzmann's constant, T is the absolute temperature, E_f is the Fermi level of the electrode on the left, V_a is the applied voltage across the double barrier structure. The variable of integration is changed from k_1 to the longitudinal energy ($E_z = \hbar^2 k_1^2/2m^*$). An I-V curve calculated by this formula is shown in the inset of fig. 3.2 in Chapter Three.

The above theory gives the basic idea of resonant tunneling. This is enough for the basic understanding and design of useful resonant tunneling devices. However, other minor effects which are neglected in the simple theory may be important in certain considerations such as the evaluation of the valley current, understanding the physics of fast modulation and switching, resonant tunneling in indirect band gap materials, etc. Therefore, a more accurate calculation should include the scattering effect from impurities, phonons, and defects, the space charge effect, and the band structure effect. As for the study of fast response of

DBRT, the temporal behavior of the electron wavefunction has to be considered. This issue will be discussed in Chapter Three. Scattering effect will be discussed in Chapter Four where an imaginary potential is used to model the scattering effect.

1.2 Development of DBRT

In this section, the development of DBRT at different stages over the last two decades will be described, including the author's contributions in recent years.

The simplest resonant tunneling structure called the double barrier structure was proposed and demonstrated by Tsu, Esaki and Chang in 1973 and 1974 [1-2]. This early demonstration shows a peak in the I-V characteristics which was explained by a simple resonant tunneling theory described above. However, due to the relatively primitive state of the technology of sample preparation, the effect could only be seen at 77°K. Application of this effect was not demonstrated until 1983 when a double barrier resonant tunneling diode was used by Sollner's group to detect and mix a 2.5 THz signal [3]. This exciting demonstration served to kick off a large research effort in DBRT.

The research efforts on DBRT after Sollner's experiment were focused on two areas: (i) estimation and reduction of the fast response time scale [4-10], and (ii) material improvement for the enhancement of the resonant tunneling effect [11-15]. The incoherent tunneling picture [4] which is totally different from the coherent picture was proposed to explain the resonant tunneling effect. Using new materials, such as AlInGaAsP [13] for

the double barrier structure and Si and InP [11,13] for the substrate was attempted and led to many successful demonstrations of large and fast resonant tunneling effect. The author's contributions in this primary stage include:

(1) First time simulation of resonant tunneling when the double barrier structure is modulated at a few THz. This work introduces a new method to simulate the tunneling of a mono-energetic electron. The ultimate frequency limit of DBRT is found which is consistent with the experimental result [5].

(2) First time epitaxial growth of DBRT on Si substrate. High current peak and valley ratio of 2.9 at room temperature was obtained which was comparable to the record (3.9) on GaAs substrate [11].

As the device technology for DBRT improved, considerable research was aimed at understanding the basic physics of the device such as the space charge effect, e-e interaction, e-phonon interaction, and other inelastic scattering, magnetic resonant tunneling, one-dimensional quantum wire DBRT, etc. [16-25]. At this stage, the author's contributions include:

(3) Simulation of tunneling escape from the quantum well inside the double barrier structure. In this work, an imaginary potential in DBRT is used to model the recombination process which is important in the tunneling time experiment [16].

(4) Discovery of the total resonant tunneling without reflection in asymmetric double barrier structure with an imaginary potential.

This work changed the concept of **impossible** total tunneling in asymmetric structure [17].

Together with the pursuit of fundamental understanding, many novel new devices [26-38] were developed, namely, Stark Effect Transistor (SET), Resonant tunneling Bipolar Transistor (RBT), Resonant Tunneling Field Effect Transistor (RTFET) and Resonant Hot Electron Transistor (RHET). The author is responsible for the development of the first series of optical resonant tunneling devices [26-30]:

(5) Resonant Tunneling quantum well Laser (RTL) [26-27].

(6) Optically-controlled Parallel resonant-Tunneling (OPT) devices [28-30].

The field of resonant tunneling continues to grow nowadays as seen from the numerous publications in various kinds of journals. This is because of the large potential of applications and possibility of discovering new physics. Many new ideas have been proposed or demonstrated in recent years. The most important driving force for this field is the fact that resonant tunneling effect can survive even when the device size becomes much smaller. Another important driving force comes from the optical processing capability demonstrated by the author [26-30] which is necessary to utilize the advanced processing power in the optical devices. Therefore, the author believes that the ultimate functional devices in the future must be based on the resonant tunneling effect.

1.3 References

Classics

[1] R. Tsu and L. Esaki, Appl. Phys. Lett. 22, 562 (1973).

[2] L. L. Chang, L. Esaki and R. Tsu, Appl. Phys. Lett. 24, 593 (1974)

[3] T. C. L. G. Sollner, W. D. Goodhue, P. E. Tannenwald, C. D. Parker and D. D. Peck, Appl. Phys. Lett. 43, 588 (1983).

Fast response

[4] S. Luryi, Appl. Phys. Lett. 47, 490 (1986).

[5] S. C. Kan and A. Yariv, J. Appl. Phys. 64, 3098 (1988).

[6] T. C. L. G. Sollner, P. E. Tannenwald, D. D. Peck and W. D. Goodhue, Appl. Phys. Lett. 45, 1319 (1983).

[7] E. R. Brown, T. C. L. G. Sollner, C. D. Parker, W. D. Goodhue, and C. L. Chen, Appl. Phys. Lett. 55, 1777 (1989).

[8] J. F. Whitaker, G. A. Mourou, T. C. L. G. Sollner and W. D. Goodhue, Appl. Phys. Lett. 53, 385 (1988).

[9] H. C. Liu, Appl. Phys. Lett. 52, 453 (1988).

[10] D. S. Pan and C. C. Meng, Appl. Phys. Lett. 61, 2082 (1987).

Materials

[11] S. C. Kan, H. Morkoç and A. Yariv, Appl. Phys. Lett. 52, 2251 (1988).

[12] C. I. Huang, M. J. Paulus, C. A. Bozada, S. C. Dudley, K. R. Evans, C. E. Stutz, R. L. Jones, and M. E. Cheney, Appl. Phys. Lett. 51, 121 (1987).

[13] T. P. E. Broekaert, W. Lee, and C. G. Fonstad, Appl. Phys. Lett. 53, 1545 (1988).

[14] T. J. Shewchuk, P. C. Chapin, P. D. Coleman, W. Kopp, R. Fischer, and H. Morkoç, Appl. Phys. Lett. 46, 508 (1985).

[15] J. R. Söderström, D. H. Chow, and T. C. McGill, IEEE EDL-11, 27 (1990).

Physics

[16] S. C. Kan and A. Yariv, J. Appl. Phys. 67, 1957 (1990).

[17] A. Sa'ar, S. C. Kan and A. Yariv, J. Appl. Phys. 67, 3892 (1990).

[18] M. Cahay, M. McLennan, S. Datta, and M. S. Lundstrom, Appl. Phys. Lett. 50, 612 (1987).

[19] H. Morkoç, J. Chen, U. K. Reddy, T. Henderson and S. Luryi, Appl. Phys. Lett. 49, 70 (1986).

[20] H. Ohnishi, T. Inata, S. Muto, N. Yokoyama, and A. Shibatomi, Appl. Phys. Lett. 49, 1248 (1986).

[21] N. Kluksdahl, A. M. Kriman, and D. K. Ferry, Superlattices and Microstructures, 5, 397 (1986).

[22] A. Zaslavsky, V. J. Goldman, D. C. Tsui, and J. E. Cunningham, Appl. Phys. Lett. 53, 1408 (1988).

[23] M. L. Leadbeater, L. Eaves, P. E. Simmonds, G. A. Toombs, F. W. Sheard, P. A. Claxton, G. Hill, and M. A. Pate, Solid-State Electronics, 31, 707 (1988).

[24] D. Z.-Y. Ting and T. C. McGill, J. Vac. Sci. Technol. B7, 1031 (1989).

[25] E. E. Mendez, E. Calleja, C. E. T. Gonçalves da Silva, L. L. Chang, and W. I. Wang, Phys. Rev. B33, 7368 (1986).

New devices

[26] I. Grave', S. C. Kan, G. Griffel, S. Wu, A. Sa'ar and A. Yariv, "A Monolithic Integration of a Resonant Tunneling Diode and a Quantum Well Semiconductor Laser," 1990 Conference on Lasers and Electro-Optices (CLEO), 21-25 May, Anaheim, California, Paper CPDP28.

[27] I. Grave', S. C. Kan, G. Griffel, S. Wu, A. Sa'ar and A. Yariv, Appl. Phys. Lett. 58, 110 (1991).

[28] S. C. Kan, S. Wu, S. Sanders, G. Griffel, and A. Yariv, J. Appl. Phys. 69 (1991).

[29] S. C. Kan, S. Sanders, G. Griffel, G. H. Lang, S. Wu and A. Yariv, Appl. Phys. Lett. (1991).

[30] S. C. Kan, S. Wu, S. Sanders, G. Griffel and A. Yariv, "Negative Photoconductivity in Double-Barrier Resonant Tunneling Diode," Annual Meeting of Optical Society of America, 4-9 November 1990, Paper TuA2.

[31] F. Capasso, S. Sen, A. Y. Cho, and D. L. Sivco, Appl. Phys. Lett. 53, 1056 (1988).

[32] A. R. Bonnefoi, T. C. McGill, and R. D. Burnham, IEEE EDL-6, 636 (1985).

[33] C. H. Yang, Y. C. Kao and H. D. Shih, Appl. Phys. Lett. 55, 2742 (1989).

[34] F. Beltram, F. Capasso, S. Luryi, S. G. Chu, A. Y. Cho, and D. L. Sivco, Appl. Phys. Lett. 53, 219 (1988).

[35] A. R. Bonnefoi, D. H. Chow, and T. C. McGill, Appl. Phys. Lett. 47, 888 (1985).

[36] F. Capasso and R. A. Kiehl, J. Appl. Phys. 58, 1366 (1985).

[37] N. Yokoyama, K. Imamura, S. Muto, S. Hiyamizu, and H. Nishi, Japanese J. Appl. Phys. 24, L854 (1985).

[38] F. Capasso, S. Sen, and A. Y. Cho, Appl. Phys. Lett. 51, 526 (1987).

1.4 Figures

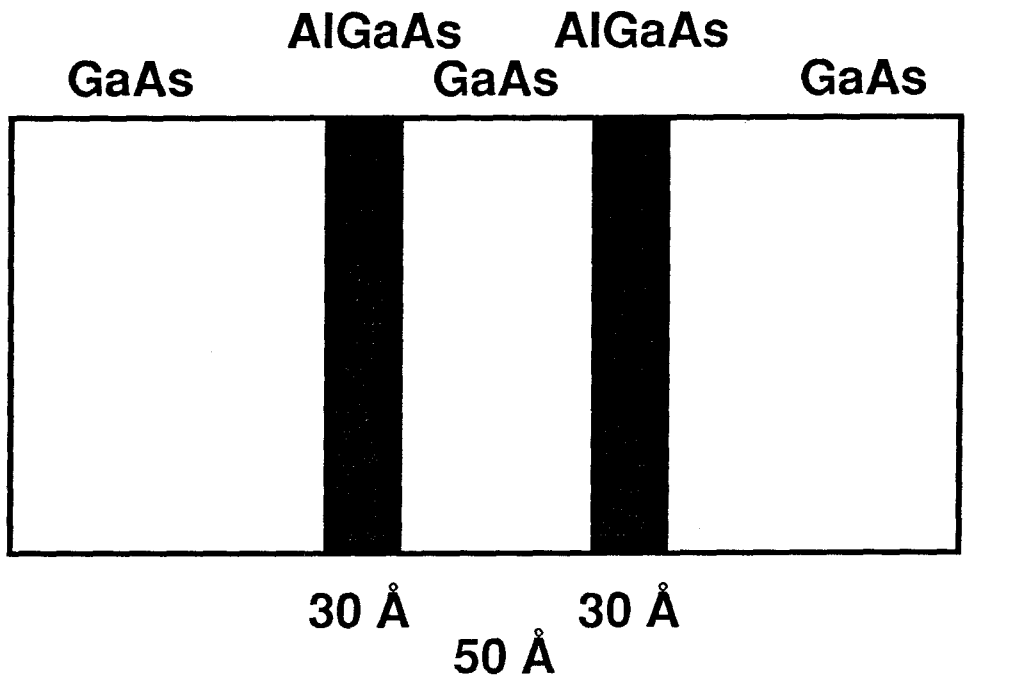

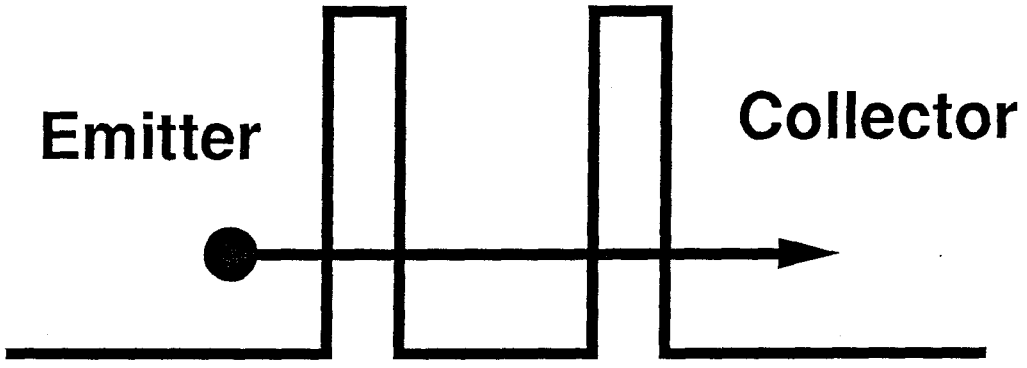

Fig. 1.1
Double Barrier Structure

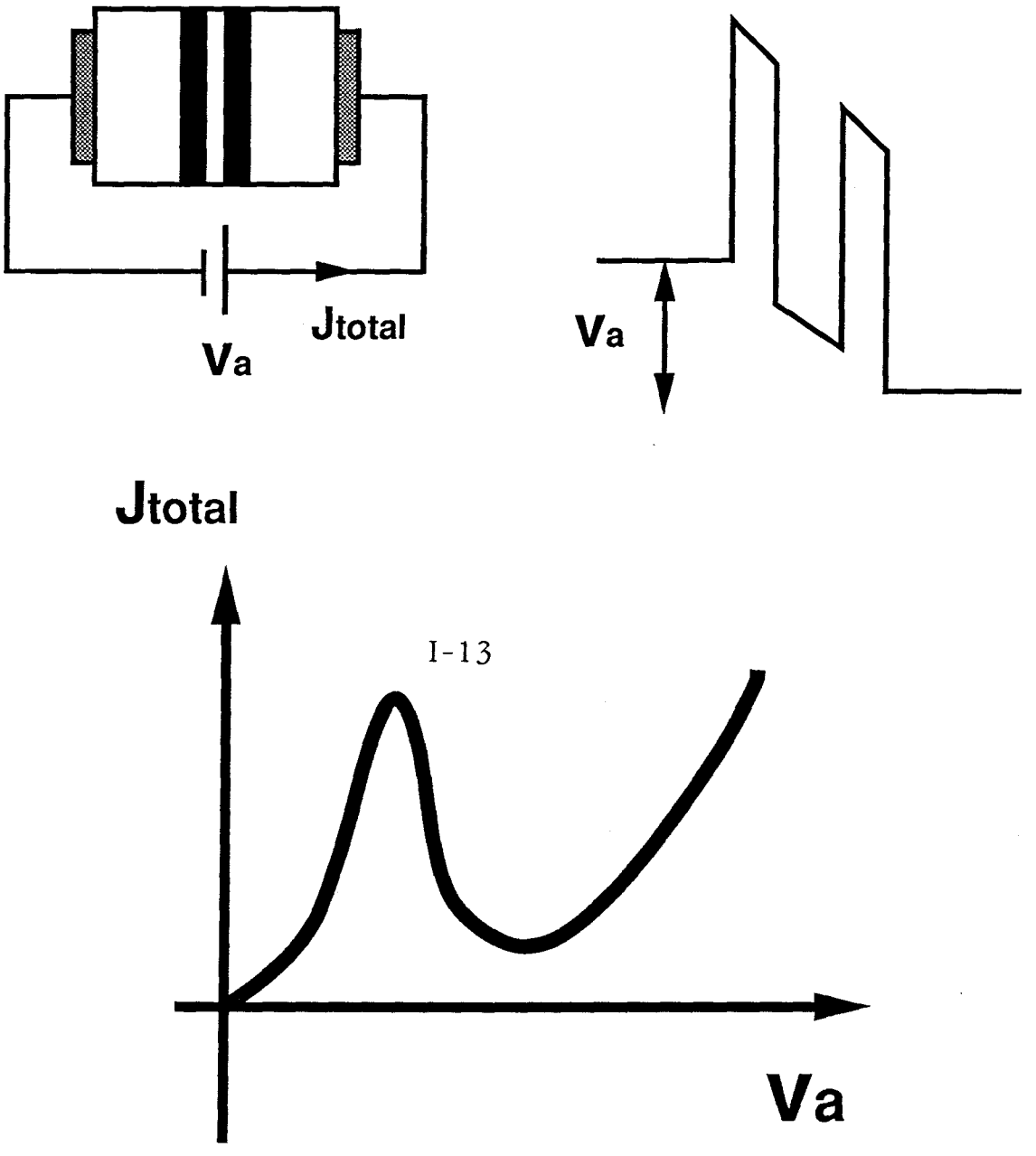

Fig. 1.2
Resonant Tunneling I-V curve

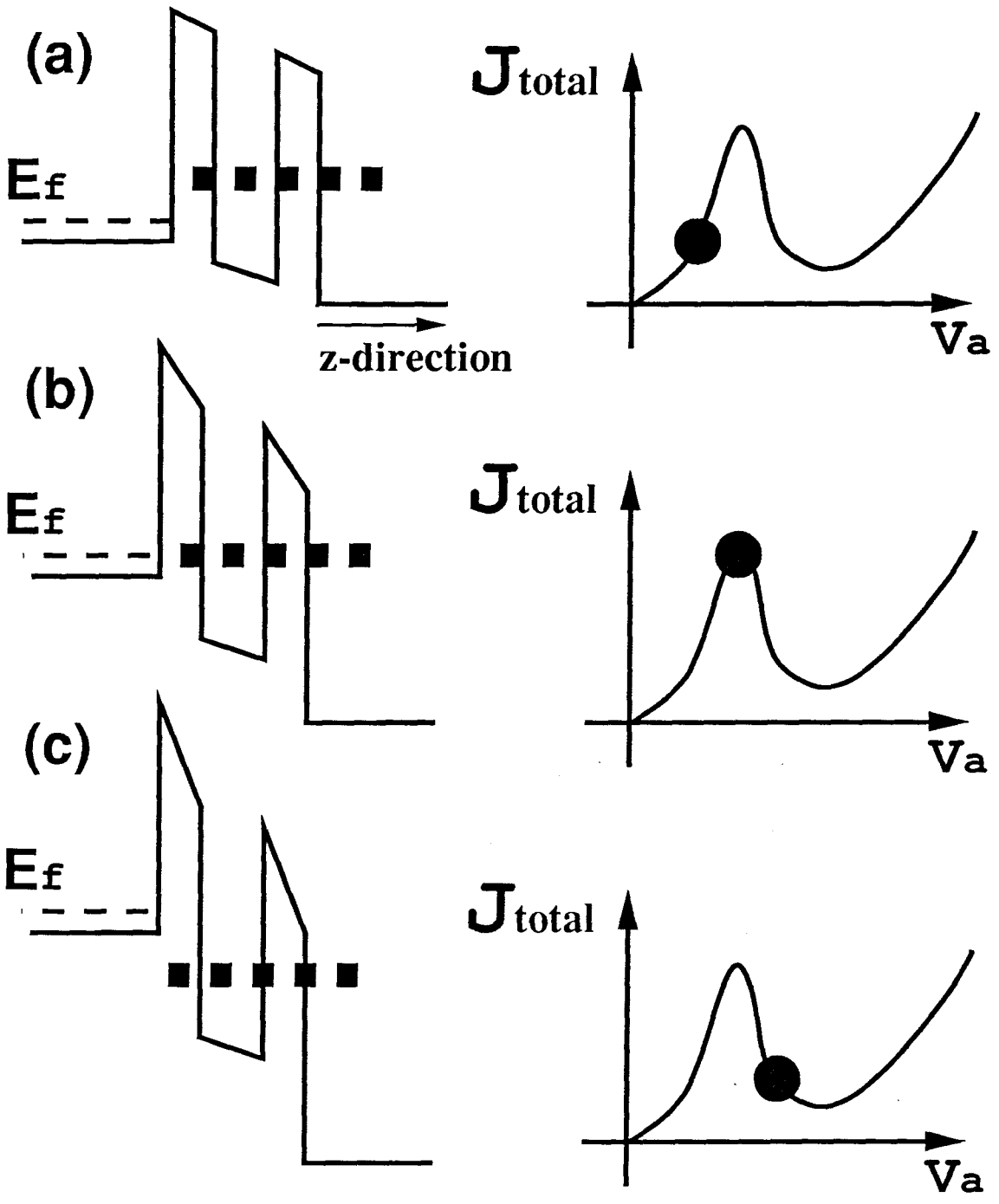

Fig. 1.3
Mechanism of Resonant Tunneling

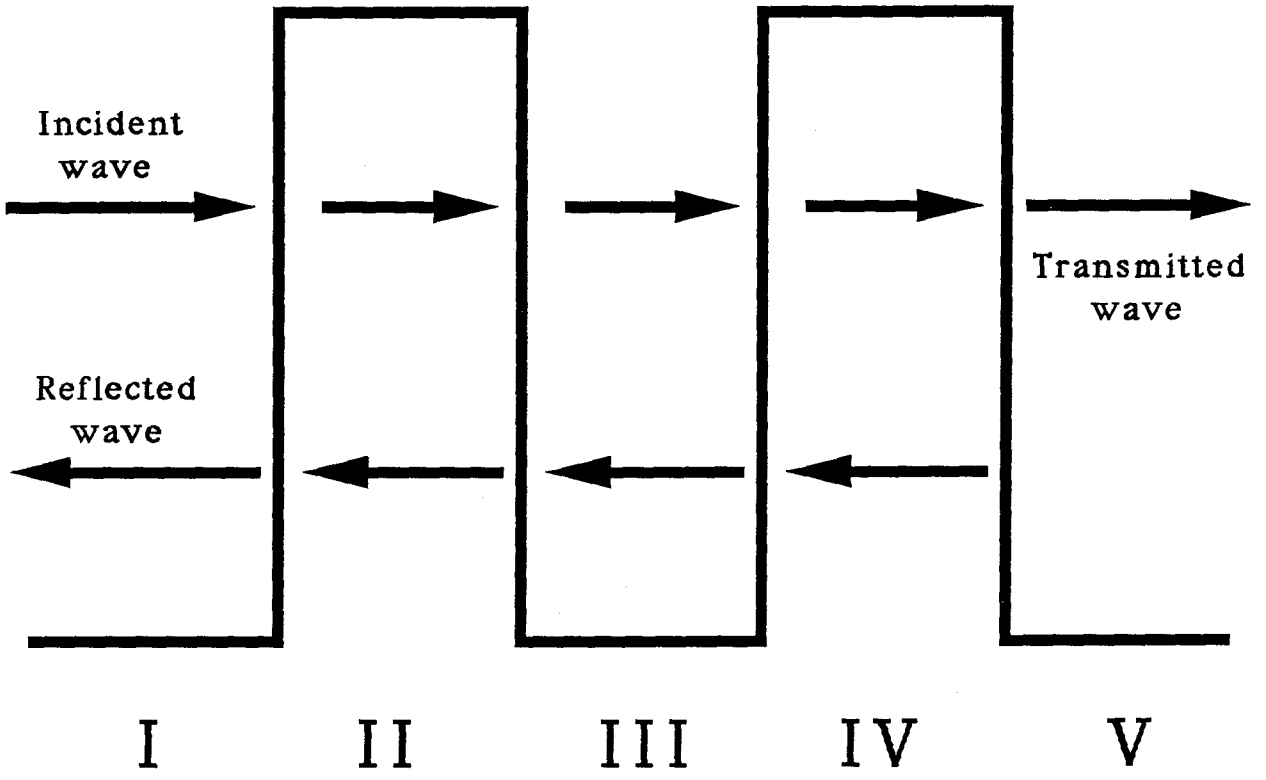

Fig. 1.4
Electronic Wavefunction
in Double Barrier Structure

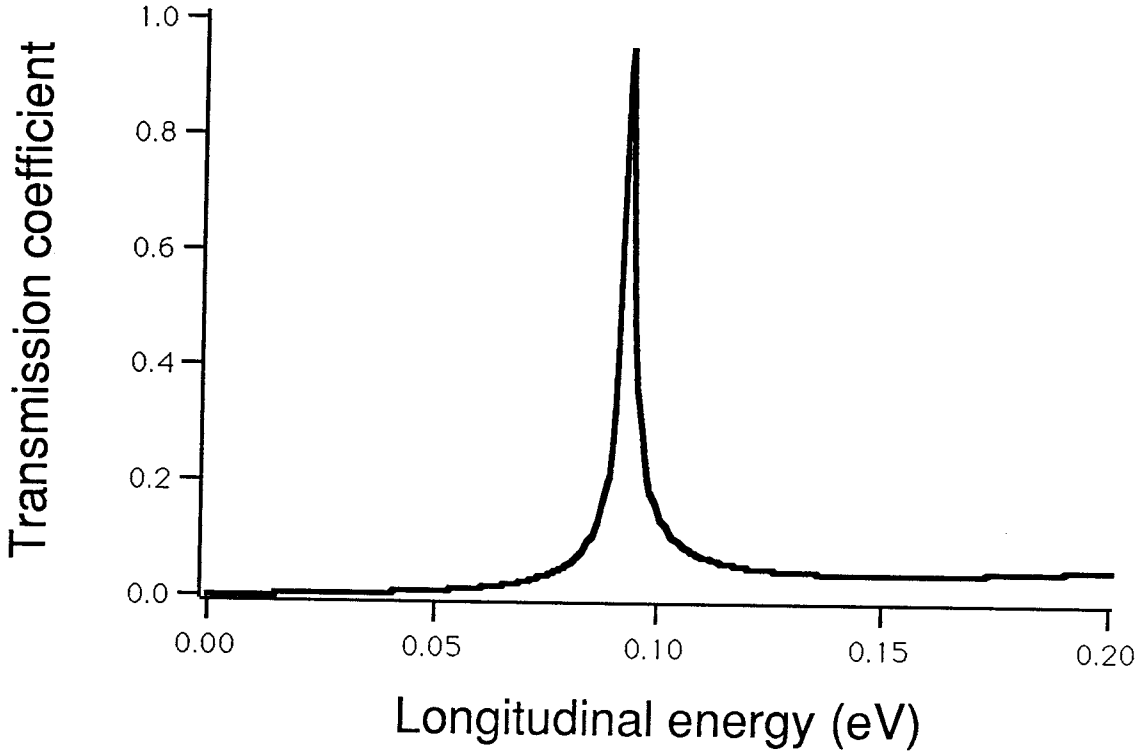

Fig. 1.5
Transmission Spectrum in Double Barrier Structure

Chapter Two

Sample Preparation of DBRT Structure on GaAs Substrate and Si Substrate by MBE

Chapter Two

Sample Preparation of DBRT on GaAs Substrate and Si Substrate by MBE

In this chapter, the sample preparation of DBRT structures by Molecular Beam Epitaxy (MBE) will be discussed. The first work using GaAs-on-Si technology to grow a GaAs DBRT structure on lattice-mismatched Si substrate will be described.

2.1 DBRT Structure Grown by MBE

Since the tunneling barriers and quantum well in DBRT structures have to be extremely thin and abrupt, only two methods at present lead to satisfactory DBRT structures. They are the Molecular Beam Epitaxy (MBE) [1-3] and Metal Organic Chemical Vapor Deposition (MOCVD) [4-5]. In our laboratory, we exclusively use MBE to prepare the DBRT structures. MBE is a technique for epitaxial growth of thin film crystals on crystalline substrates. The distinctive feature of a MBE system shown in fig. 2.1 is the capability to perform layer-by-layer epitaxial growth. In a typical MBE growth, the substrate is put in front of the effusion cells. The molecular beams from the effusion cell react on the substrate surface and form the crystal extension of the substrate. Since the growth process is layer-by-layer, the growth can be easily controlled, and very abrupt (mono-layer accuracy) heterojunctions and doping profiles can be obtained.

Although DBRT structures can be prepared by growing several heterojunctions as in fig. 1.1 in a straightforward manner, the tricks to prepare a good DBRT structure, however, take years to develop [6-15]. As described in Chapter One, DBRT structures have been produced by MBE as early as 1974 [6]. However, the technology to prepare a good substrate and produce an abrupt and high quality heterojunction was not up to the task and the resonant tunneling effect could be observed only at 77°K. The most important steps in preparing a good DBRT structure are the growth of high purity undoped double barrier structure [7] and the introduction of spacer to prevent the Si impurity migration into the structure as shown in fig. 2.2 [8]. Other important steps include the introduction of growth interruption at the heterojuncntion interface, and incorporation of strained layer and deep quantum well using InGaAs [9-15]. All these efforts lead to the success of room temperature resonant tunneling effect and fast response demonstration. Using different strained layer and deep quantum well further enhances the resonant tunneling effect and using new materials such as InSb improves the response time.

2.2 GaAs-on-Si Technology

As the technology of growing DBRT structures on lattice-matched GaAs substrate became mature, the effort was shifted to prepare DBRT structures on the practical but lattice-mismatched Si substrates [11]. In this section, the technology of growing GaAs epitaxial layers on Si substrates by MBE will be reviewed.

Epitaxial growth of GaAs on Si substrate has been extensively studied in recent years [16-20]. Electronic and optical devices from this composite structure have been fabricated for novel applications [21-25]. The resultant devices make it possible to combine the advantages of GaAs/AlGaAs and Si monolithically, i.e., the optical devices from GaAs/AlGaAs and mature electronic circuits and devices from Si can be operated on the same chip. Other advantages of using Si material are that Si is less brittle, has higher thermal conductivity which is essential to dissipate heat efficiently, and has a smaller defect density compared to GaAs. However, there are several critical problems of growing GaAs epitaxial layers on Si substrate:

(1) One problem is the anti-phase. Because of the polar nature of GaAs crystal and the nonpolar nature of Si crystal, it is very difficult to have uniform Ga layer and As layer over a large area on the wafer surface. Unwanted change from Ga atoms to As atoms on the same layer is called anti-phase problem as is shown in fig. 2.3. An arsenic prelayer before the growth of GaAs and slow initial growth rate of GaAs were used to alleviate this problem. The substrate temperature was set between 400 and 500°C at the initiation of the growth with a 7 sec of As_2 exposure prior to gallium flux. The growth rate and the substrate temperature were then increased to 1 μm/hr and 600°C respectively in 20 minutes during the first 200 Å of growth.

(2) Another problem is the dislocation spreading. Because of the 4% lattice mismatch between GaAs and Si crystal, a significant amount of dislocations are developed at the GaAs-Si interface. A tilted substrate is

used to alleviate this problem. The substrate used to demonstrate the first GaAs DBRT structures on Si is an n-type Si wafer tilted by 4 degrees towards the (110) direction. Strained layer superlattice is also used to bend the propagation direction of dislocation in order to reduce the number of dislocations which will extend to the layers for the device structure.

2.3 GaAs-DBRT-on-Si

The high performance of quantum well devices grown on Si, e.g., quantum well lasers and modulation doped field effect transistors (MODFET) has demonstrated that device quality epitaxial layers can be obtained on Si. However, a DBRT device based on perpendicular and coherent quantum transport is more difficult to prepare because the electron wavefunction has to extend coherently over a wide region away from the double barrier structure. Therefore, in order to obtain a large resonant tunneling effect, a wide region of high crystalline quality is required. In the following, we describe the first GaAs DBRT structure grown on Si substrate by MBE using the techniques mentioned above.

The DBRT layered structure is as follows:

(1) a GaAs spacer of 1000 Å
(2) an AlAs barrier of 20 Å
(3) a GaAs quantum well of 56 Å
(4) an AlAs barrier of 20 Å
(5) a GaAs spacer of 1000 Å

The entire structure is lightly doped to $10^{16}\,cm^{-3}$ with Si. A 0.2 μm n type (Si, $10^{18}\,cm^{-3}$) top GaAs electrode was grown on top of the double barrier structure. Growth rates of GaAs and AlAs layers were 1 and 0.5 μm/hr, respectively. A 2 μm n type Si, 10^{18} cm^{-3} GaAs buffer layer was grown to smooth out any imperfection before the growth of the DBRT structure.

The cleaning procedure included a degreasing in TCE, removal of heavy metals in nitric acid/sulphuric acid (volume ratio is 1:1), a series of oxide growth in HCℓ/water/peroxide (volume ratio is 3:5:3) and stripping steps in HF/water (volume ratio is 1:10), and a last oxide growth. The oxide was then desorbed in the MBE chamber at 1000°C for about one minute.

A circular mesa of 50 μm diameter shown in fig. 2.4 was fabricated by chemical etching. The current-voltage (I-V) characteristics were measured by an I-V tracer. The deviation of the peak and valley currents for all the diodes fabricated is only about 10% indicating high uniformity and crystalline quality over large areas. The largest current peak to valley ratio is 2.9 and 12.5 at room temperature and 77°K (fig. 2.5), respectively. The diode with the largest negative resistance has a peak current density of 1600 A/cm^2 and valley current density of 550 A/cm^2 at room temperature. At 77°K, the peak current density increased to 2500 A/cm^2 and valley current density decreased to 200 A/cm^2. The current peak to valley ratio of 2.9 at room temperature is comparable to the best result (3.9) obtained from devices grown on GaAs substrates.

2.4 Conclusions

In conclusion, we have successfully prepared the first GaAs DBRT structure on Si substrate. The current peak to valley ratio of 2.9 at room temperature was fairly high as compared to the record of 3.9 on GaAs substrates, indicating the material quality of the epitaxial layers grown on Si substrate is comparable to that on GaAs substrates. This important step makes the integration of GaAs resonant tunneling devices with the well-developed Si devices possible. Complex functional devices based on this achievement should be foreseeable in the future.

2.5 References

MBE

[1] A. Y. Cho, The Technology and Physics of MBE, edited by E. H. C. Parker, 1st edition, Plenum Press, New York, Chapter One, 1985.

[2] B. A. Joyce, Rep. Prog. Phys. 48, 1637-1697 (1985).

[3] W. T. Tsang, Semiconductors and Semimetals, vol. 22, Part A, Chapter Two (1985).

MOCVD

[4] H. M. Manasevit and W. I. Simpson, J. Electrochem. Soc. 116, 1725 (1969).

[5] R. D. Dupuis, P. D. Dapkus, R. D. Yingling, and L. A. Moudy, Appl. Phys. Lett. 31, 201 (1978).

MBE growth of DBRT Structures

[6] L. L. Chang, L. Esaki and R. Tsu, Appl. Phys. Lett. 24, 593 (1974).

[7] T. C. L. G. Sollner, P. E. Tannenwald, D. D. Peck, and W. D. Goodhue, Appl. Phys. Lett. 45, 1319 (1984).

[8] M. Tsuchiya and H. Sakaki, Appl. Phys. Lett. 49, 88 (1986).

[9] T. Inata, S. Muto, Y. Nakata, S. Sasa, T. Fujii, and S. Hiyamizu, Jpn. J. Appl. Phys. 26, L1332 (1987).

[10] C. H. Yong and H. D. Shih, Elect. Lett. 24, 553 (1988).

[11] S. C. Kan, H. Morkoç and A. Yariv, Appl. Phys. Lett. 52, 2251 (1988).

[12] C. I. Huang, M. J. Paulus, C. A. Bozada, S. C. Dudley, K. R. Evans, C. E. Stutz, R. L. Jones, and M. E. Cheney, Appl. Phys. Lett. 51, 121 (1987).

[13] T. P. E. Broekaert, W. Lee, and C. G. Fonstad, Appl. Phys. Lett. 53, 1545 (1988).

[14] T. J. Shewchuk, P. C. Chapin, P. D. Coleman, W. Kopp, R. Fischer, and H. Morkoç, Appl. Phys. Lett. 46, 508 (1985).

[15] J. R. Söderström, D. H. Chow, and T. C. McGill, IEEE EDL-11, 27 (1990).

GaAs on Si

[16] W. I. Wang, Appl. Phys. Lett. 44, 1149 (1984).

[17] W. T. Masselink, T. Henderson, J. Klem, R. Fischer, P. Pearah, H. Morkoç, M. Hafich, P. D. Wang and G. Y. Robinson, Appl. Phys. Lett. 45, 1309 (1984).

[18] R. Fischer, W. T. Masselink, J. Klem, T. Henderson, T. C. McGlinn, M. V. Klein, H. Morkoç, J. H. Mazur, and J. Washburn, J. Appl. Phys. 58, 374 (1985).

[19] N. Otsuka, C. Choi, L. A. Kolodziejski, R. L. Gunshor, R. Fischer, C. K. Peng, H. Morkoç, Y. Nakamura and S. Nakagura, J. Vac. Sci. Technol. B4, 896 (1986).

[20] B. G. Yacobi, S. Zemon, P. Norris, C. Jagannath and P. Sheldon, Appl. Phys. Lett. 51, 2236 (1987).

Devices from GaAs on Si

[21] H. Z. Chen, A. Ghaffari, H. Morkoç, A. Yariv, Appl. Phys. Lett. 51, 2094 (1987).

[22] H. K. Choi, B-Y Tsaur, G. M. Metze, G. W. Turner and J. C. C. Fan, IEEE EDL-5, 205 (1984).

[23] R. Fischer, T. Henderson, J. Klem, W. T. Masselink, W. Kopp, H. Morkoç and C. W. Litton, Electron. Lett. 20, 945 (1984).

[24] R. J. Fischer, J. Klem, C. K. Peng, J. S. Gedymin and H. Morkoç, IEEE EDL-7, 112 (1986).

[25] H. Morkoç, J. Chen, U. K. Reddy and T. Henderson and S. Luryi, Appl. Phys. Lett. 49, 70 (1986).

2.6 Figures

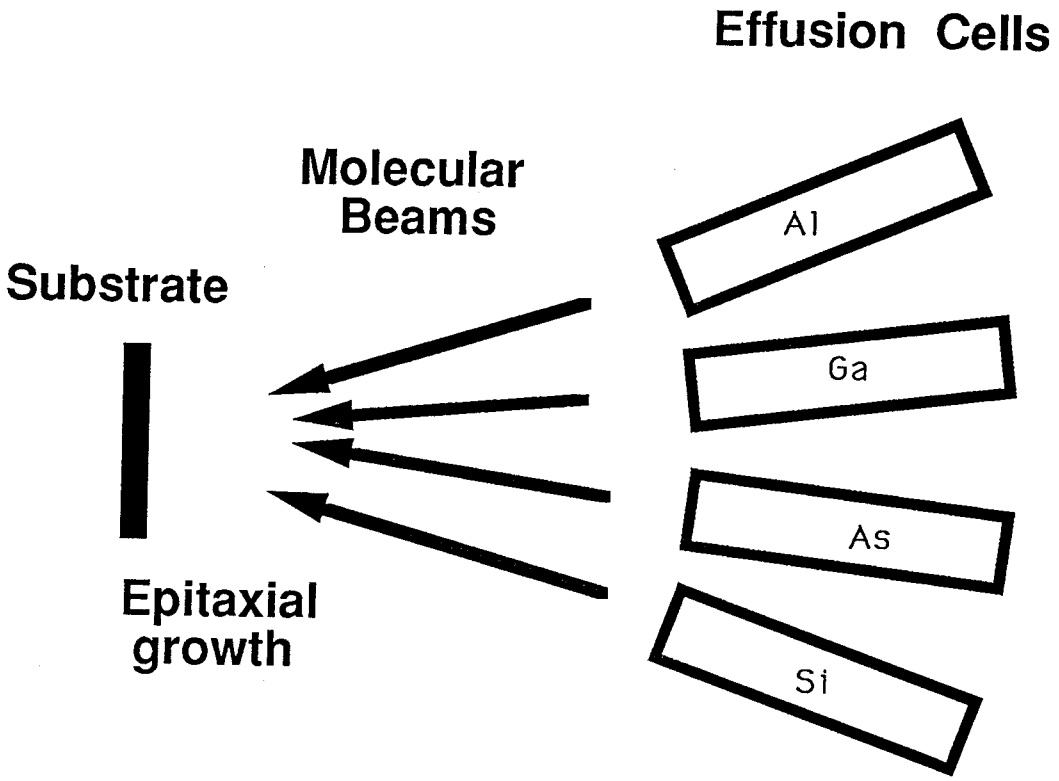

Fig. 2.1
MBE Growth

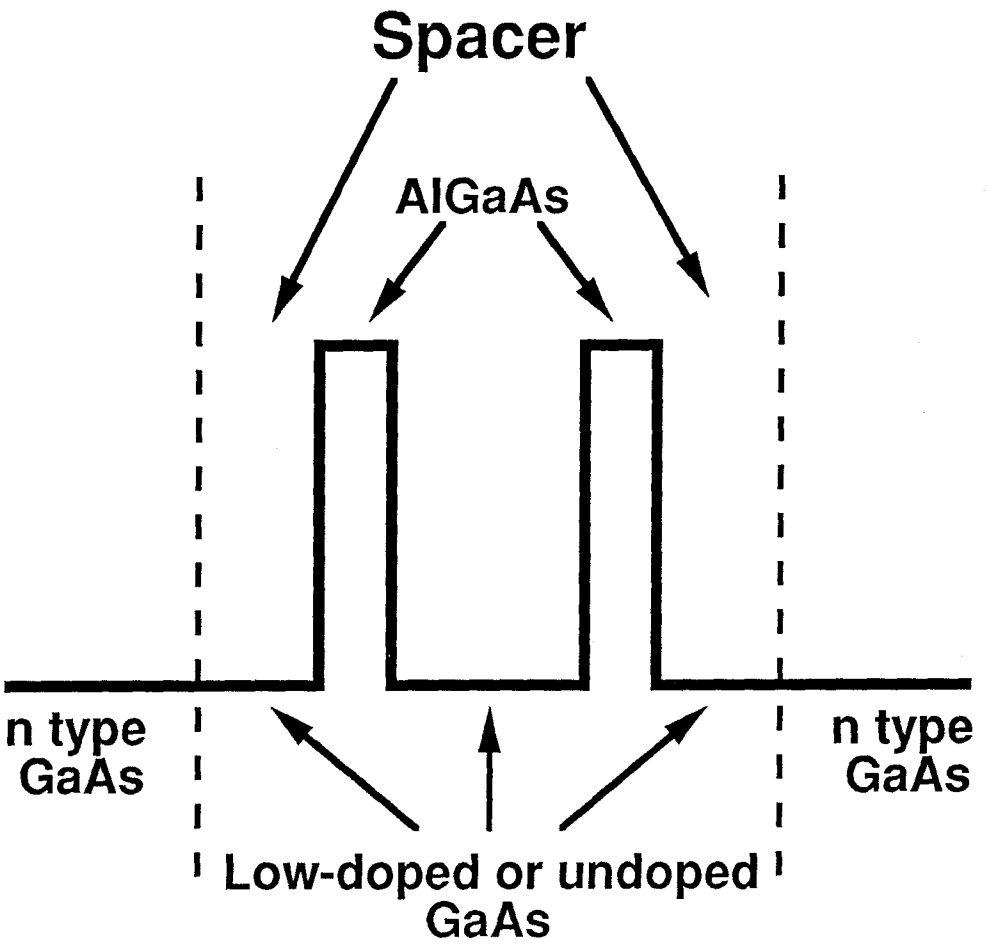

Fig. 2.2
Spacer in DBRT structure

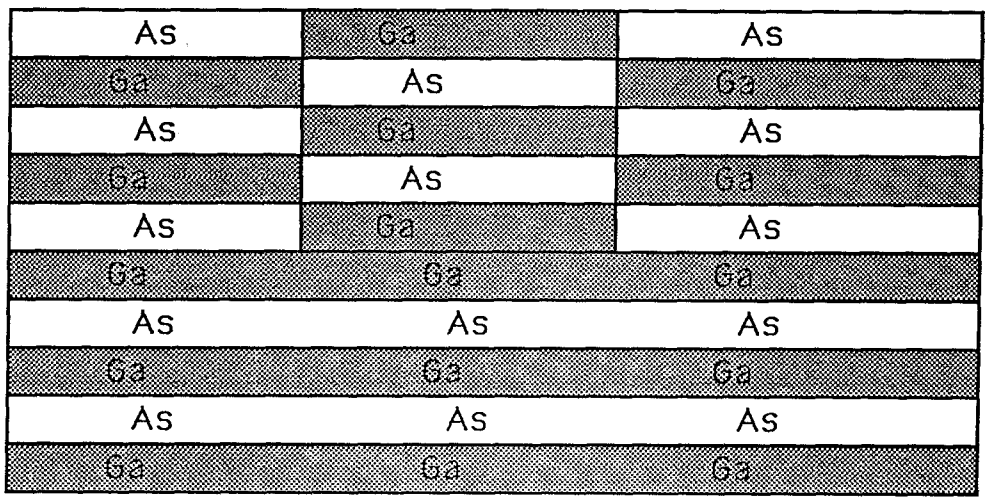

Fig. 2.3
Anti-phase problem

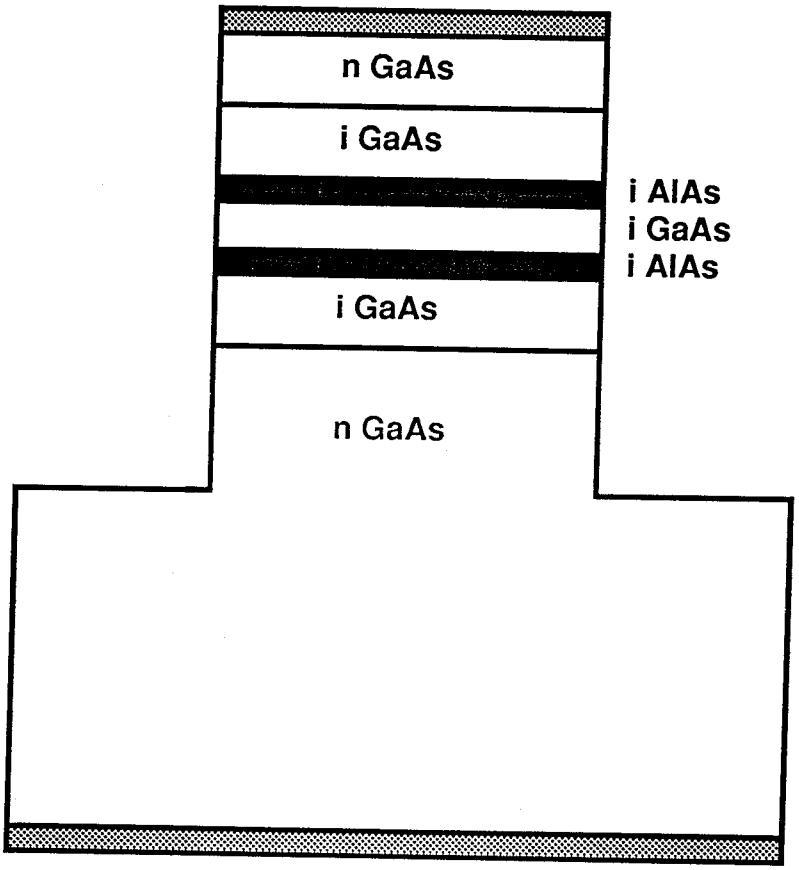

Fig. 2.4
Mesa structure

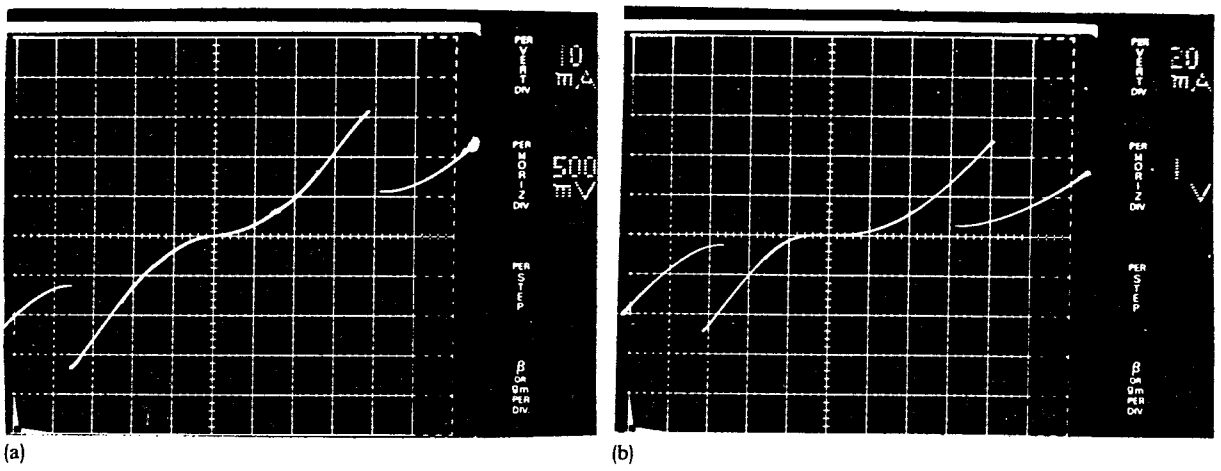

300°K 77°K

Fig. 2.5
Experimental I-V Curve of the First GaAs DBRT on Si Substrate

Chapter Three

Tera Hertz Modulation of DBRT

Chapter Three

Tera Hertz Modulation of DBRT

In this chapter, the issue of high frequency modulation of DBRT structure at a few tera hertz will be addressed. A new approach to treating the problem of the frequency response at high frequency modulation will be introduced. Using the new approach, we determine the frequency limit of DBRT and reveal the details of the tunneling in the fast modulated structure.

One of the major advantages of DBRT is that the resonant tunneling effect can be obtained even when the double barrier structure is modulated at very high frequency [1-5]. Modulation of DBRT at low frequencies can be treated by using the static DBRT theory discussed in Chapter One. When the modulation time scale is comparable to the intrinsic tunneling time, a dynamical DBRT theory is needed to describe the time-dependent DBRT. The frequency response of the DBRT will be studied by a new approach in this chapter.

3.1 Simulation of DBRT at High Frequency Modulation

In this section, a new approach is introduced to simulate the DBRT at very high frequency modulation [6]. The frequency response of the DBRT is determined from the simulation result. The model structure in our study is a typical symmetric double barrier structure similar to the device on which the fastest operation was reported. It is composed of two 22.5 Å

wide $Al_{0.3}Ga_{0.7}As$ barriers and a 52.5 Å wide GaAs quantum well. The barrier height is 0.24 eV. The structure is sandwiched between GaAs electrodes which are n-doped to $5 \times 10^{17}/cm^3$. The temperature is 77°K.

The modulation of the double barrier structure is described as follows. A voltage drop $V_a(t)$ is applied across the structure as shown in fig. 3.1. This voltage drop is changed in time in the following way:

$$V_a(t) = V_b \qquad \text{for } t < 0,$$

$$V_a(t) = V_b + V_m \sin(\omega t) \qquad \text{for } t > 0.$$

That is, when $t < 0$, the potential is static and when $t > 0$, the double barrier structure is modulated periodically in time.

The values of V_b and V_m are chosen in the following way. We first calculate the static I-V curve of the device using the formula derived in Chapter One:

$$J = \frac{e\,m^*\,k\,T}{2\pi^2\hbar^2}\int_0^\infty |a_{51}|^2 \frac{k_5}{k_1} \log\left\{\frac{1+\exp[(E_f-E_z)/kT]}{1+\exp[(E_f-E_z-eV_a)/kT]}\right\} dE_z \qquad (3.1)$$

which is plotted in the inset of fig. 3.2. The parameters in equation (3.1) are defined in Chapter One after equations (1.1) and (1.2). The I-V curve in fig. 3.2 indicates that the negative conductance is largest when V_a = 0.15V. Since the point with largest negative conductance is usually chosen to be the operation point in most applications, we choose V_b to be 0.15V. We also choose V_m to be 0.01V so that the operation point will sweep through most of the negative conductance region on the I-V curve.

We consider a mono-energetic electron plane wave incident on this modulated structure. For $t < 0$, the electron wavefunction is the eigenstate of the time-independent structure since the potential is static. For $t > 0$, the wavefunction will evolve according to the time-dependent Schrödinger equation:

$$\hbar\, i \frac{\partial \Psi(z,t)}{\partial t} = -\frac{\hbar^2}{2m^*} \frac{\partial^2 \Psi(z,t)}{\partial z^2} + V(z,t)\, \Psi(z,t)$$

where $\hbar = h/2\pi$ and h is Planck's constant, $\Psi(z,t)$ is the electron wavefunction, and V(z,t) is the modulated double barrier potential which depends on $V_a(t)$ as shown in fig. 3.1.

The electron energy is chosen in the following way. First, we re-examine the current expression (3.1). The integrand in the expression is the current distribution due to the electrons with different longitudinal energy (E_Z) which is plotted in fig. 3.2. The area under the distribution corresponds to the total current. Several curves corresponding to the structure with different applied voltage V_a are plotted. The position of the dominant part (i.e., the peak) of the distribution changes significantly in the positive resistance region from V_a=0.12 volt to 0.14 volt. But for the negative resistance region from V_a=0.14 volt to 0.17 volt, which is of great interest, the peak of the distribution does not change much and the main effect from the increase of V_a is the decrease in the overall area. This means that the electrons with longitudinal energy, E_Z, ranging from 0 to 10 meV make a dominant contribution to the change of the total current. This narrow spectrum also suggests that simulation of these electrons will give meaningful information about the resonant tunneling. Hence, in our study, we pick the longitudinal energy of our model electron to be 4 meV.

The eigenfunction with E_Z = 4 meV, which is the initial wavefunction, is then calculated. The time evolution of the wave function is then obtained by solving the time-dependent Schrödinger equation based on the effective mass approximation [7]. The wavefunction Ψ and its first spatial derivative $d\Psi/dz/m^*$ are matched at each interface. The time-dependent Schrödinger equation is solved using the Crank-Nicolson implicit scheme [8] which is described in the appendix. The local current of the wavefunction can be calculated from the local current operator in equation (1.1).

3.2 Simulation Results

In this section, the simulation results will be presented. The simulations at different modulation frequencies (f=385 GHz, 770 GHz, 1.54 THz, 3.08 THz, 6.16 THz) are performed. The probability density and current at different places (ρ_{peak}, ρ_1, ρ_2 and $J_T(t)$ shown in fig. 3.3) as a function of time are plotted in fig. 3.4. The results are categorized as follows:

3.2.1 General dynamics

According to fig. 3.4, the evolution of the wavefunction is summarized as follows. Before t = 0, the wavefunction is the eigenfunction which involves incident, reflected and transmitted plane waves. After t = 0, we find that the "old" transmitted and reflected plane waves, which leave the structure before t = 0, propagate in the same way as in a time-independent system. But for the plane wave incident on the structure

after t = 0, the "new" transmitted and reflected waves change in amplitude. The sum of the transmitted current and reflected current is not necessarily equal to the incident current because of the charging and discharging processes of the quantum well which correspond to the on and off of DBRT in time. The changes of the transmitted wave and reflected wave are propagating away from the double barrier structure. Hence, the current in the left and right electrodes is also changing with time. The change of the wavefunction undergoes **a transient stage** and then **a periodic modulation** following the varying potential. The amplitude of the periodic modulation of the wavefunction decreases with frequency and from this, the ultimate frequency limit is determined.

3.2.2 Frequency response

Simulation results show that the amplitude of the periodic modulation of the wavefunction decreases with the modulation frequency. Here we focus on the transmitted current density at the right edge of the second barrier, $J(z=z_2, t)$ which is denoted by $J_T(t)$ in fig. 3.3. The relative values, $J_T(t)/J_T(0)$ for different frequencies are plotted in fig. 3.4. The linear and nonlinear frequency responses are calculated in the following way. We expand $J_T(t)$ into a Fourier series:

$$J_T(t) = \sum_{n=0}^{\infty} [\, a_n \cos(n\omega t) + b_n \sin(n\omega t) \,]$$

The linear response (c_1) is taken as $\sqrt{a_1^2 + b_1^2}$ corresponding to the first harmonic, and the nonlinear response (c_2) is taken as $\sqrt{a_2^2 + b_2^2}$ corresponding to the second harmonic. The linear response (c_1) and

nonlinear response (c_2) as a function of frequency are plotted in fig. 3.5. The linear response (c_1) starts decreasing above 1.54 THz and is down by 50% at 3.08 THz and displays a 1/f dependence at high frequency. This is consistent with the experimental result of 2.5 THz response in Ref. 3. The nonlinear response (c_2) also starts decreasing above 1.54 THz but an enhancement at 770 GHz is observed.

3.2.3 Charging and discharging

One important effect of the modulation is the charging and discharging process in the double barrier structure. Since the spatial profile of the probability density inside the quantum well is generally bell shaped, the total probability inside the quantum well is roughly proportional to the peak value of the probability density, $|\Psi(z,t)|^2_{max}$ which is denoted by $\rho_{peak}(t)$ in fig. 3.3. The relative value, $\rho_{peak}(t)/\rho_{peak}(0)$, is also plotted in fig. 3.4 for different frequencies.

To shed more light on the the charging and discharging process, the local current near the double barrier structure at different times within one period of the modulation is plotted in fig. 3.6 for the 1.54 THz case. The current varies in space which signifies charge accumulation and depletion. The slope inside the quantum well is changing from positive to negative and vice versa in time. From the continuity equation, we know that the positive and negative slopes correspond to the discharging or charging process, respectively. The steeper slope inside the quantum well compared to the slope in the barriers or electrodes means the charging and discharging rates are faster in the quantum well.

3.2.4 Transmitted pulses - On and Off of DBRT

By plotting the probability density to the right of the second barrier in fig. 3.7, we observe the generation of the transmitted pulses due to the on and off resonance during a modulation period. The width of the pulse, about 5000 Å, corresponds to a spread of about 1 THz in the energy of the electron. This is about the same as the modulation frequency of 1.54 THz. This is also the evidence of the scattering to higher energy states and lower energy states with a quantum of $\hbar\omega$ absorbed and emitted as considered by time dependent scattering theory [5]. An unexpected phenomenon is that the pulses do not disperse but are compressed. The peak of the pulse is increasing at a constant rate and the width of the pulse is decreasing. This is probably due to overtaking of the early "slow" charge by the late "faster" charge as the kinetic energy of the electron is modulated.

3.3 Conclusions

In conclusion, we have developed a new method to simulate the resonant tunneling when the double barrier structure is modulated at a few THz. The simulation results explicitly show that the resonant tunneling effect diminishes when the modulation frequency is increased. This determines the ultimate frequency limit of double barrier resonant tunneling.

3.4 References

[1] T. C. L. G. Sollner, E. R. Brown, W. D. Goodhue and H. Q. Le, Appl. Phys. Lett. 50, 332 (1987).

[2] D. D. Coon and H. C. Liu, Appl. Phys. Lett. 49, 94 (1986).

[3] D. S. Pan and C. C. Meng, Appl. Phys. Lett. 61, 2082 (1987).

[4] E. R. Brown, W. D. Goodhue, and T. C. L. G. Sollner, J. Appl. Phys. 64, 1519 (1988).

[5] H. C. Liu, Appl. Phys. Lett. 52, 453 (1988).

[6] S. C. Kan and A. Yariv, J. Appl. Phys. 64, 3098 (1988).

[7] G. Bastard and J. A. Brum, IEEE QE-22, 1625 (1986).

[8] Steve E. Koonin, Computational Physics, First Edition, page 161, Benjamin/Cummings, Menlo Park (1986).

3.5 Figures

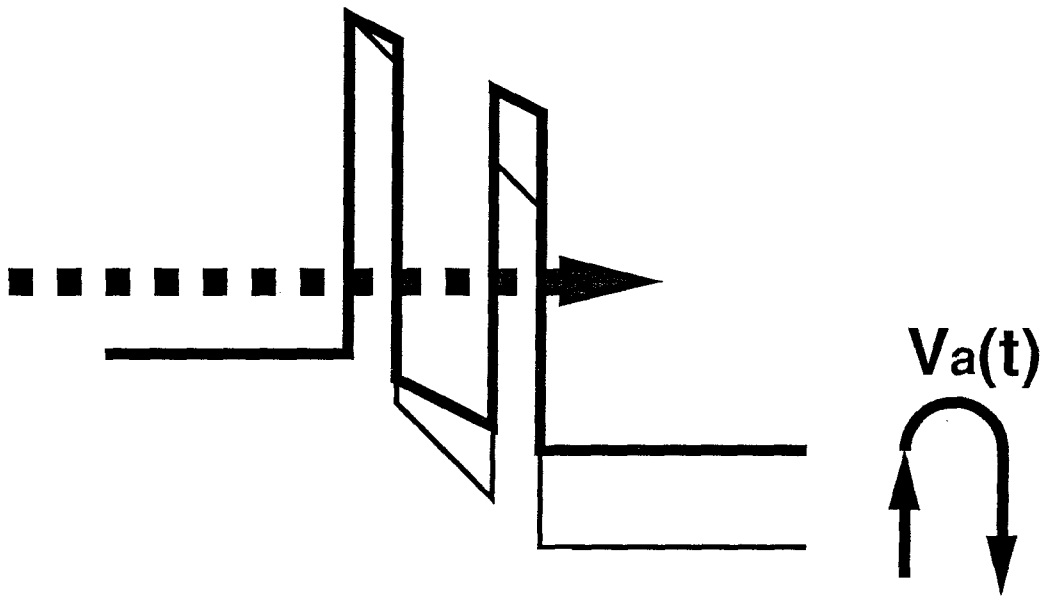

$$V_a(t) = V_b + V_m \sin(wt)$$

Fig. 3.1
Modulation of Double Barrier Structure

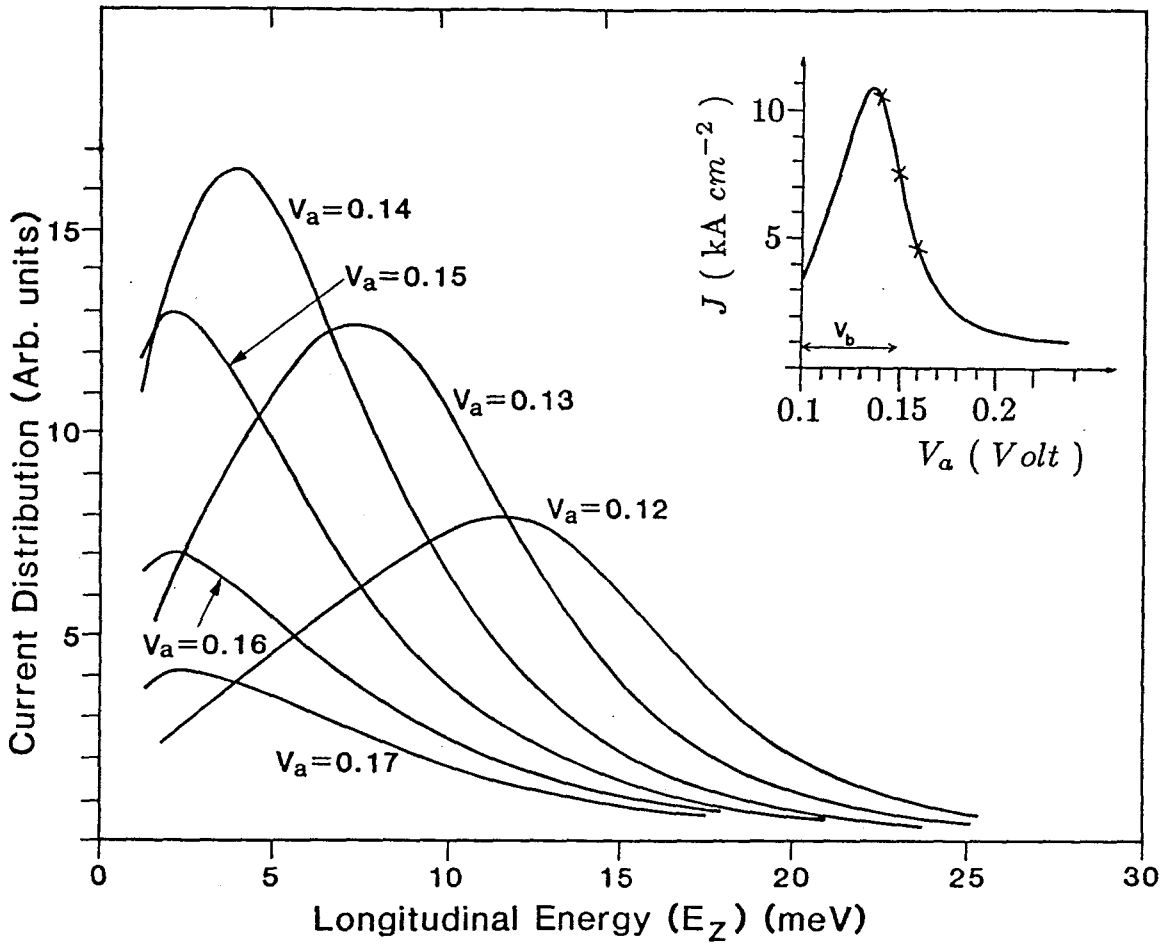

Fig. 3.2
Change of the Current Spectrum

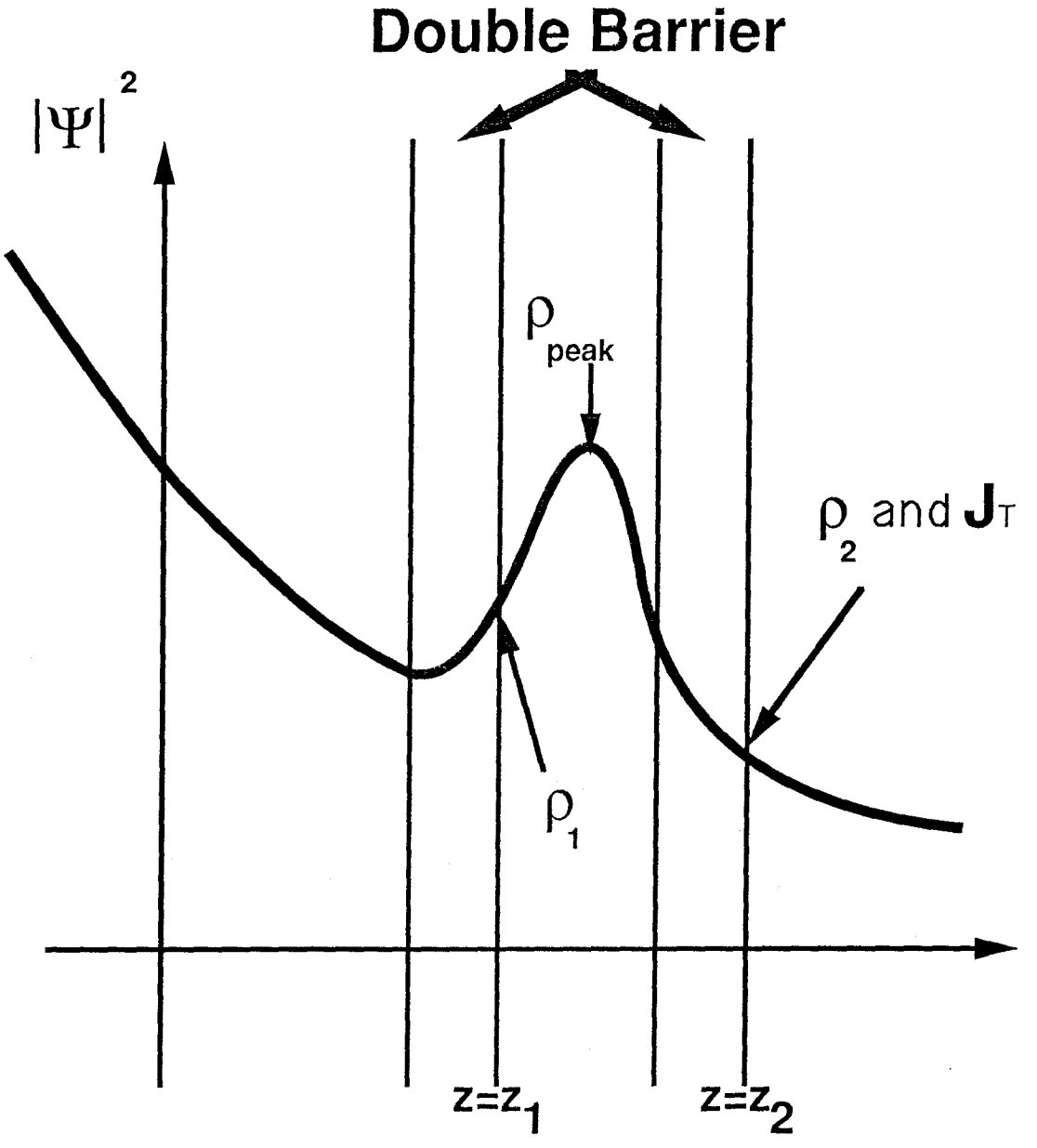

Fig. 3.3
Electronic Wavefunction in Double Barrier Structure

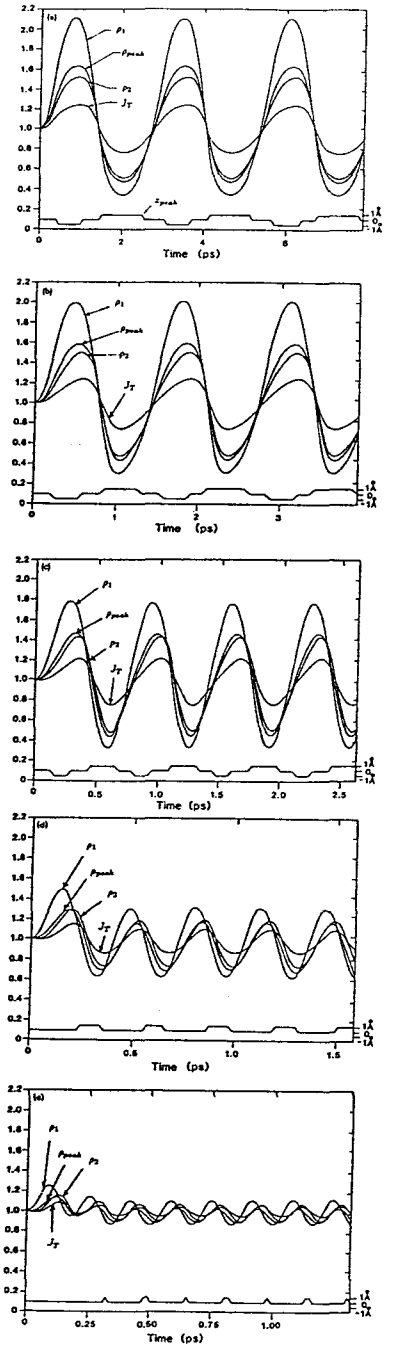

0.385 THz

0.77 THz

1.54 THz

3.08 THz

6.16 THz

Fig. 3.4
Evolution of the Wavefunction

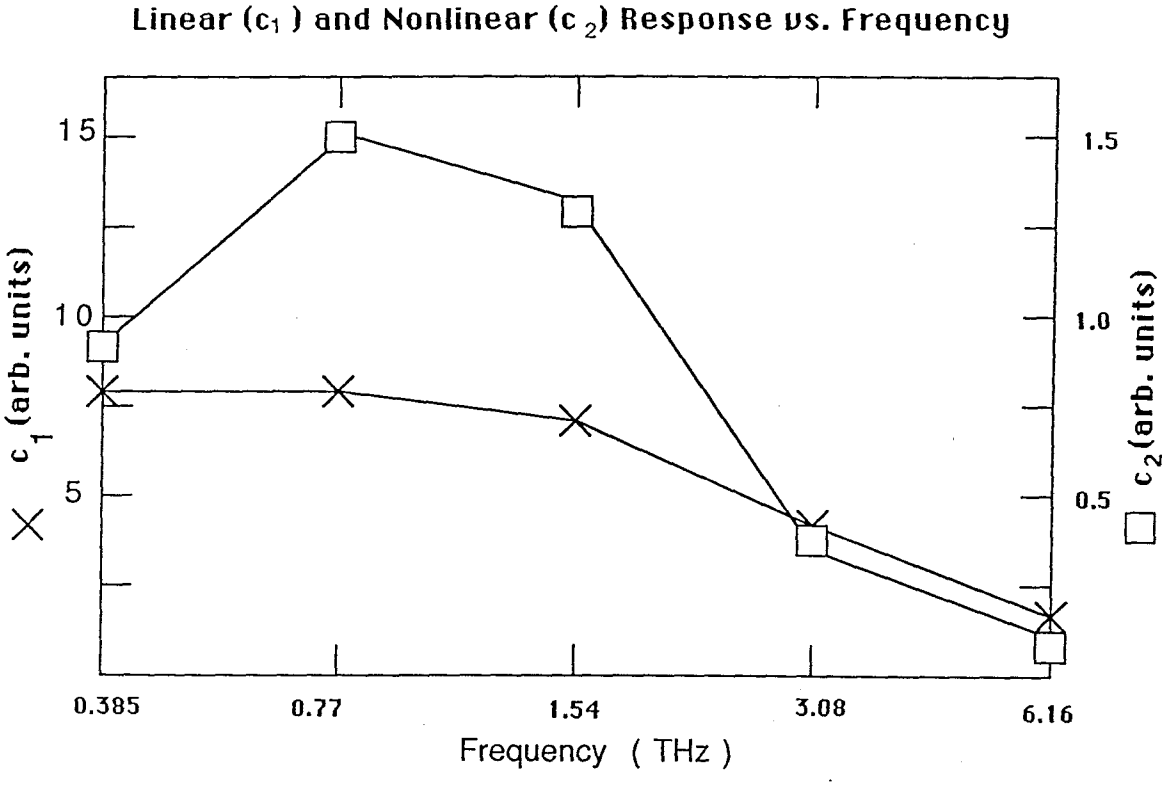

Fig. 3.5
Frequency Response of Resonant Tunneling

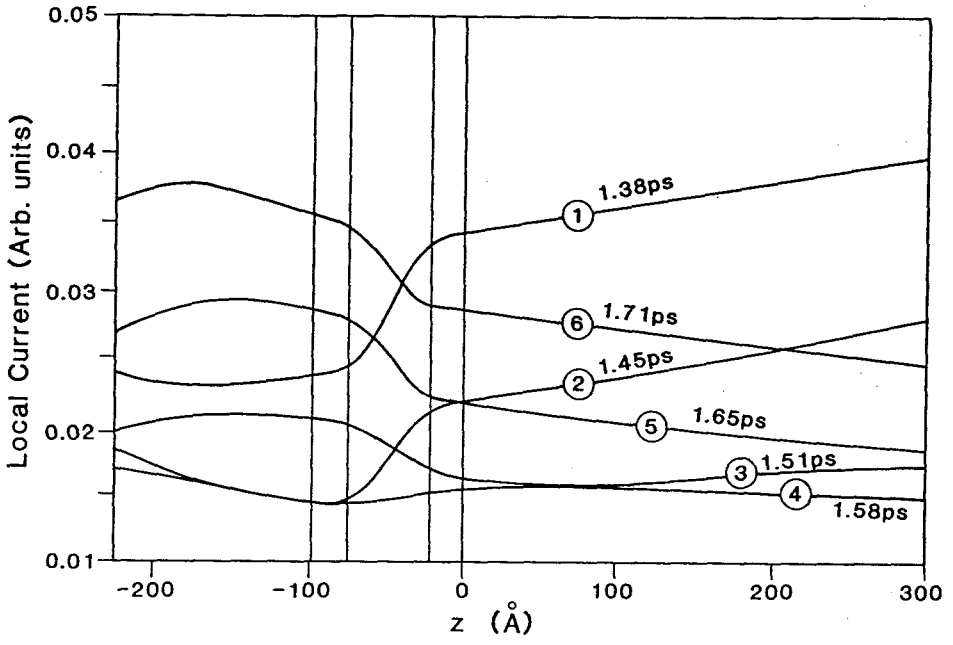

Fig. 3.6
Probability Current Density in Double Barrier Structure

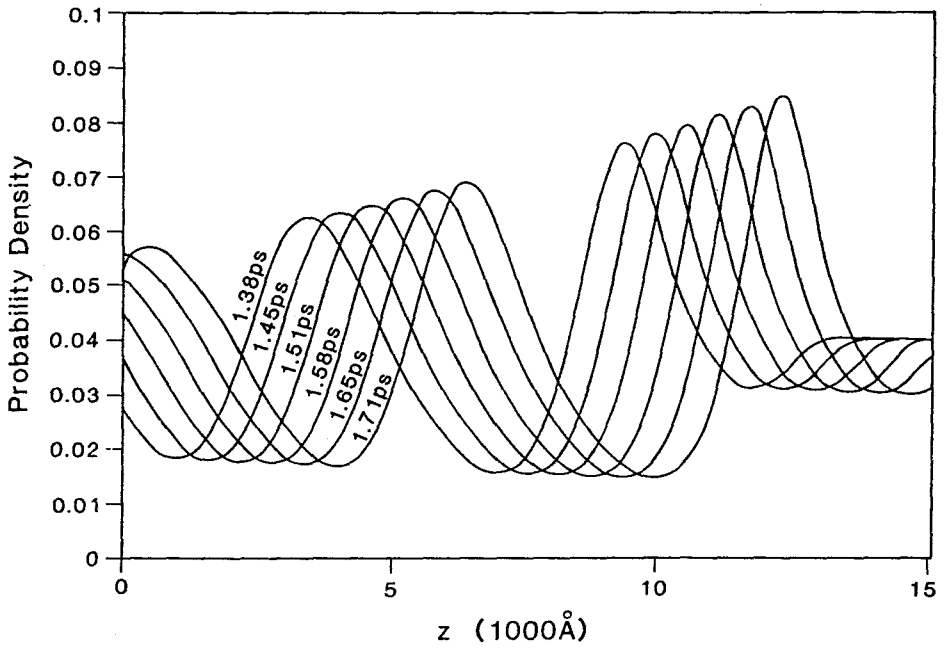

Fig. 3.7
Outgoing Probability Wave from Double Barrier Structure

Chapter Four

Imaginary Potential in DBRT

Chapter Four

Imaginary Potential in DBRT

The imaginary potential is a phenomenological tool for describing the scattering loss of a particle. This concept was introduced by Niels Bohr at the early stage of Quantum Mechanics [1]. In many-body theory, it is used to understand the concept of quasi-particle [2]. The imaginary potential was used by Stone and Lee in 1985 to study the inelastic scattering effect on DBRT in 1985 [3]. This method, in general, is very useful in treating the scattering loss effect in DBRT [4-5]. In this chapter, the general properties of a Hamiltonian with an imaginary potential are discussed. Two applications of imaginary potential to DBRT system are illustrated. One is to model the recombination process by the imaginary potential in the simulation of tunneling time experiment. Another one is to model the general scattering processes in the study of asymmetric double barrier structure.

4.1 Non-hermitian Hamiltonians

The eigenvectors of a hermitian operator with different eigenvalues are known to be orthogonal to each other and all the eigenvalues are real numbers [6]. Here, we re-examine the overlap integral of two eigenvectors of a non-hermitian Hamiltonian with different eigenvalues. First, we write down the time-independent Schrödinger equation for an eigenvector $|1\rangle$:

$$\left[H_0 - i\, V^{im}(x)\right] |1\rangle = E_1 |1\rangle \qquad (4.1)$$

and the hermitian conjugate of the equation for another eigenvector $|2\rangle$:

$$\langle 2| \left[H_0 + i\, V^{im}(x) \right] = E_2^* \langle 2| \tag{4.2}$$

where H_0 is a hermitian potential, $V^{im}(x)$ is the imaginary potential which is assumed to be positive, E_1 and E_2 are the eigenvalues. By making an inner product of $|1\rangle$ with equation (4.2) and an inner product of $\langle 2|$ with equation (4.1), and then taking the difference, we get:

$$-2\, i\, V_{21}^{im} = (E_1 - E_2^*) \langle 2|1\rangle \tag{4.3}$$

where $V_{21}^{im} = \langle 2|\, V^{im}(x)\, |1\rangle$. The overlap integral between $|2\rangle$ and $|1\rangle$ becomes:

$$\langle 2|1\rangle = \frac{-2\, i\, V_{21}^{im}}{E_1 - E_2^*} \tag{4.4}$$

V_{21}^{im} is non-zero in general and hence $|2\rangle$ is not orthogonal to $|1\rangle$ although $E_1 \neq E_2$.

Next we examine the eigenvalues of the Hamiltonian. By setting $|2\rangle = |1\rangle$ in equation (3), we get the imaginary part of the eigenvalue:

$$Im\,(E) = -\frac{V_{11}^{im}}{\langle 1|1\rangle} \tag{4.5}$$

Since V_{11}^{im} and $\langle 1|1\rangle$ are positive, Im(E) is negative. This gives an exponential decay of the amplitude of the wavefunction with time since:

$$e^{-i(E/\hbar)t} = e^{-i[Re(E)/\hbar]t}\, e^{-[Im(E)/\hbar]t} \tag{4.6}$$

where $\hbar = h/2\pi$ and h is Planck's constant. This is exactly the property of a quasi-particle in the many-body theory. However, a distinction has to be made between extended states and localized states. For localized states, $\langle 1|1\rangle$ is unity and therefore, $Im\,(E) = -V_{11}^{im}$ which is nonzero in general. But for the extended states, $\langle 1|1\rangle$ is infinite. If $V^{im}(x)$ is localized within some region, V_{11}^{im} is finite and therefore, Im(E) is zero. Im(E) can have non-

zero value only if $V^{im}(x)$ is not localized which corresponds to a large recombination bath in the bulk material. Therefore, for extended states, the eigenvalues of a Hamiltonian with a localized imaginary potential are real numbers.

4.2 Non-conservation of Matter

Now, we examine how the non-orthogonality of extended states is related to non-conservation of matter. We construct a normalizable wave packet from the superposition of extended eigenfunctions, $|k\rangle$ with the eigenvalue $E_k \equiv \hbar\omega_k$,

$$\Psi(x,t) = \int_{-\infty}^{\infty} A(k)\,|k\rangle\, e^{-i\omega_k t} dk \tag{4.7}$$

with $\langle\Psi(x,0)|\Psi(x,0)\rangle = 1$. The norm of $\Psi(x,t)$ becomes:

$$\langle\Psi(x,t)\,|\,\Psi(x,t)\rangle = \int_{-\infty}^{\infty}\int_{-\infty}^{\infty} A^*(k')\,A(k)\langle k'|\,k\rangle\, e^{-i(w_k - w_{k'})t}\, dk\, dk' \tag{4.8}$$

Note that the only time dependence of $\langle\Psi(x,t)|\Psi(x,t)\rangle$ comes from the nonzero contribution of $\langle k' \mid k\rangle$ when $k \neq k'$ which is $-2i V^{im}_{kk'} / (E_k - E_{k'})$. For a hermitian Hamiltonian, $\langle k' \mid k\rangle = \delta(k-k')$ and hence, $\langle\Psi(x,t)|\Psi(x,t)\rangle$ is time-independent. Therefore, the non-orthogonality of the eigenvectors is responsible for the non-conservation of matter.

The loss of matter through the imaginary potential becomes more apparent in the continuity equation derived from the time dependent Schrödinger equation:

$$\hbar\, i\, \frac{\partial \Psi(x,t)}{\partial t} = -\frac{\hbar^2}{2m^*}\, \nabla^2 \Psi(x,t) + \left[V(x) - i\, V^{im}(x)\right]\, \Psi(x,t) \tag{4.9}$$

where V(x) is the real potential. The continuity equation becomes:

$$\frac{\partial \rho(x,t)}{\partial t} = -\, \nabla \cdot J(x,t) - \frac{2}{\hbar}\, V^{im}(x)\, \rho(x,t) \tag{4.10}$$

where $J = (\hbar/2\, m^*\, i)\, (\Psi^* \nabla \Psi - \Psi \nabla \Psi^*)$. The last term in equation (4.10) corresponds to a sink for the probability density.

4.3 Application of Imaginary Potential (I)

In this section, the imaginary potential is used in the numerical simulation of the tunneling time experiment. In the tunneling time experiment, the electrons inside the quantum well in the double barrier structure are excited from the valence band to the conduction band. By measuring the recombination rate, one can estimate how fast these photoexcited electrons can escape from the double barrier structure. Here we use the imaginary potential to model the recombination process inside the quantum well and simulate the dynamics of the photo-excited electrons. The lifetime of these photo-excited electrons is measured from the simulation results.

4.3.1 Quasi-bound state in double barrier structure

The electrons inside the quantum well of the double barrier structure have a finite lifetime because of the finite tunneling escape amplitude. This lifetime, which is related to the tunneling time, can be measured experimentally by picosecond time-resolved photoluminescence

technique [7-9]. In the experiment, the electrons inside the quantum well were photo-excited from the valence band to the conduction band. These electrons proceed to either tunnel from the quantum well or recombine with the holes inside the quantum well emitting photons as shown in fig. 4.1. The luminescence intensity was measured in the experiment as a function of time and the tunneling rate can be found by assuming the following rate equation:

$$\frac{1}{\tau_{tun}} = \frac{1}{\tau_{total}} - \frac{1}{\tau_{recom}} \tag{4.11}$$

where τ_{tun} is the tunneling escape time, τ_{recom} is the recombination time and τ_{total} is the total lifetime of the electron measured from the decay of luminescence intensity. This experimental method introduces a recombination channel inside the quantum well so that the electron tunneling cannot be simulated without taking the amplitude of the wavefunction in the valence band into account. A simpler approach is to model the recombination process by a localized imaginary potential. In this way, the simple picture of the wavefunction, which consists of the amplitude in the conduction band only, can be maintained. The imaginary potential, $V^{im}(x)$, is shown in fig. 4.1 and fig. 4.2. $V^{im}(x)$ is taken to be constant (Γ) inside the quantum well and to be zero in the barriers and outside the structure. The localization of the imaginary potential corresponds to a localized density of holes inside the quantum well. Numerical simulation of the electron tunneling in such a complex potential is demonstrated in the next section.

4.3.2 Simulation of tunneling escape

In this section, we simulate the tunneling escape of the photo-excited electrons inside the quantum well in the double barrier structure by directly solving the time-dependent Schrödinger equation [10]:

$$\hbar\, i \frac{\partial \Psi(x,t)}{\partial t} = -\frac{\hbar^2}{2m^*}\frac{\partial^2 \Psi(x,t)}{\partial x^2} + [\, V^{real}(x) - i\, V^{imag}(x)\,]\, \Psi(x,t)$$

where $\Psi(x,t)$ is the electron wavefunction, $V^{real}(x)$ is the double barrier potential and $V^{imag}(x)$ is the localized imaginary potential as in fig. 4.2. The simulation method is described in Chapter Three.

An initial localized wavefunction is constructed as follows. First we calculate the resonance energy at the peak in the transmission spectrum and then the resonance eigenfunction, $\Phi_{res}(x)$, of a double barrier structure without the imaginary potential. The initial wavefunction for the simulation is constructed by multiplying this resonance eigenfunction by a Gaussian envelope so that it is localized in the quantum well:

$$\Psi(x,t=0) = B\, e^{-(x/\Delta)^2}\, \phi_{res}(x)$$

where B is the normalization constant and Δ is a constant for the localization of the wavefunction.

Two different symmetric structures with different barrier width L_b (fig. 4.2) are considered. Both structures have a quantum well of 64 Å and barrier height of 0.96 eV. L_b = 21 Å and 32 Å, respectively. In order to study the time scale for the tunneling and recombination processes, we define several time-dependent quantities:

(1) The total integrated density:

$$q(t) \equiv \int_{-\infty}^{\infty} |\Psi(x,t)|^2 dx$$

(2) The integrated density inside the structure:

$$q_{in}(t) \equiv \int_{-b}^{b} |\Psi(x,t)|^2 dx$$

(3) The integrated density outside the structure:

$$q_{out}(t) \equiv q(t) - q_{in}(t)$$

where x=-b and b are the positions of the barriers shown in fig. 4.2. q(t), $q_{in}(t)$ and $q_{out}(t)$ are plotted as a function of time for L_b=21 Å in fig. 4.3a and for L_b=32 Å in fig. 4.3b. Decay of these quantities in time is observed.

In order to compare the decay time scale with the theoretical estimation, we calculate the transmission spectrum of the double barrier structure with and without the imaginary potential. We denote the width of the resonance peaks as $\Delta E_{\Gamma\neq 0}$ and $\Delta E_{\Gamma=0}$ for the structure with and without the imaginary potential, respectively. Half width at half maximum is taken in the calculation. The tunneling escape time scale (τ_{tun}) is taken to be $\hbar/\Delta E_{\Gamma=0}$. The total lifetime (τ_{total}) of the electron inside the quantum well is taken to be $\hbar/\Delta E_{\Gamma\neq 0}$. The recombination time (τ_{recom}) is taken to be $\hbar/\Gamma$ which is 66 ps in this simulation.

For the structure with L_b=21Å, we found that $\Delta E_{\Gamma=0} = 3.8\times10^{-4}$ eV and $\Delta E_{\Gamma\neq 0} = 4.0\times10^{-4}$ eV. Therefore, τ_{tun} = 1.7 ps and τ_{total} = 1.6 ps. These two time scales should correspond to the decay time of $q_{in}(t)$. As seen in fig. 4.3a, $q_{in}(t)$ decays from about 100% to about 40% in 1.6 ps. There is very small difference for the cases with Γ=0 and $\Gamma\neq 0$. This agrees with the small difference between 1.7 ps and 1.6 ps.

For the structure with L_b=32Å, we found that $\Delta E_{\Gamma=0}$ = 2.7x10^{-5} eV and $\Delta E_{\Gamma\neq0}$ = 4.2x10^{-5} eV. Therefore, τ_{tun} = 24 ps and τ_{total} = 16 ps. As seen in fig. 4.3b, $q_{in}(t)$ decays from about 100% to about 40% in about 24 ps for Γ=0 and in about 14 ps for $\Gamma\neq0$. This also agrees with the estimation.

The evolution of the total "charge", q(t), is of interest. As seen in fig. 4.3a&b, q(t) remains unity for Γ=0 because of the conservation of matter and decreases with time for $\Gamma\neq0$ because of the loss of matter through recombination. Since the loss of q(t) corresponds to the recombination, -dq/dt should be proportional to the luminescence intensity observed in the experiment [7]. In fig. 4.4, we plot -dq/dt as a function of time. The faster decay of -dq/dt for L_b=21Å is due to the faster tunneling escape of electrons from the quantum well and hence the smaller chance to recombine in the quantum well. These results agree qualitatively with the experimental results.

4.4 Application of Imaginary Potential (II)

In this section, the imaginary potential is used to study the resonant tunneling in asymmetric double barrier structure. Tunneling with zero reflection was shown to be impossible in asymmetric double barrier structure [11]. In the following, we will describe a discovery of the possible total tunneling without reflection in a double barrier structure in the presence of a localized imaginary potential. In section 4.4.1, the interpretation of the imaginary potential in this study will be explained. In section 4.4.1, the effect of the imaginary potential on the resonant tunneling in asymmetric structures will be presented.

4.4.1 Modeling of scattering by imaginary potential

As discussed in section 1.4, the simple tunneling theory introduced in Chapter One is only an approximation to the real system. Due to some kinds of imperfection of the system like lattice vibrations, impurities, and other kinds of defects, scattering processes different from the resonant scattering from the double barrier potential may exist. These scattering processes can destroy the coherency of the wavefunction, which is essential to the resonance. This leads to the incoherent tunneling or sequential tunneling picture [12-14]. Those scattering processes essentially remove the probability density of the electron from the original wavefunction, which transports coherently across the double barrier structure.

In this study, we model all those other scattering mechanisms by a potential with a small imaginary part. In this way, the removal or decay of the probability density of the electron can be described. The magnitude of the imaginary potential (Γ), in the first approximation, is taken to be $\hbar/\tau$ where τ is the time scale for those scattering mechanisms which can be either calculated from the first principle [15] or measured by experiments [16].

4.4.2 Effect on asymmetric structure

The effects of the imaginary potential on the reflection and transmission spectra ($|r(E)|^2$ and $|t(E)|^2$), the resonance width and the resonance energy of an asymmetric double barrier structure are studied in

this section. The potential of the double barrier structure is plotted in fig. 4.5. The structure consists of an AlAs barrier with a thickness (b_1), a 53 Å wide GaAs quantum well, and another AlAs barrier with a thickness (b_2). Barrier height is 0.96 eV. Effective mass in GaAs is 0.067 m_0 and in AlAs is 0.19 m_0 where m_0 is free electron mass. The imaginary potential, $V^{im}(x)$ shown in fig. 4.5, is zero outside the quantum well and is constant (-i Γ) inside the quantum well. The magnitude (Γ) is taken to be positive which corresponds to a loss of matter through the imaginary potential as explained in section 4.2. The interface conditions are the continuity of Ψ and $(d\Psi/dx)/m^*$ where Ψ is the wavefunction and m^* is the effective mass.

The first asymmetric structure to be studied has b_1=21Å and b_2=27Å. The $|r(E)|^2$ and $|t(E)|^2$ of this structure with an imaginary potential at different magnitudes (Γ=0 eV, 1.4 x 10^{-6} eV, 1.385 x 10^{-5} eV and 1.4 x 10^{-4} eV) are plotted in fig. 4.6. As shown in the figure, the minimum of $|r(E)|^2$, denoted by $|r(E)|^2_{min}$, drops when Γ increases from zero. The $|r(E)|^2_{min}$ becomes **zero** at a certain value of Γ . It then increases when Γ further increases. In fig. 4.7, $|r(E)|^2_{min}$ is plotted against Γ . Five structures are studied. b_1=21Å for all structures and b_2= ∞Å, 27Å, 23Å, 21Å, 20Å respectively. Zero reflection was observed for those structures with $b_2 > b_1$. We denote the value of Γ, at which $|r(E)|^2_{min}$ becomes zero, by Γ_0. The dependence of Γ_0 on b_2 is plotted in fig. 4.8. Γ_0 approaches a constant value when b_2 approaches infinity and drops to zero when $b_2 = b_1$.

The change of the polarity of Γ_0 when b_2 becomes smaller than b_1 can be understood in the following way. The zero reflection is a

consequence of the totally destructive interference between the reflections from the barriers. If the two barriers are not the same, the reflections cannot be totally cancelled out. Therefore, it is impossible to have total tunneling without reflection in asymmetric double barrier structure. However, in a double barrier structure with a localized imaginary potential inside the quantum well, the imaginary potential helps to compensate the difference of the reflections from two barriers. The polarity of the compensation changes when the polarity of the difference of the barriers changes and hence, Γ_0 changes sign.

As seen in fig. 4.6, the resonance position does not change with Γ for all structures. The peak transmission, i.e., the maximum of $|t(E)|^2$, is found to decrease with Γ in all the structures. The resonance width (ΔE), i.e., the half width at half maximum of the resonance peak, is broadened according to the formula: $\Delta E = \Delta E_{\Gamma=0} + \Gamma$ where $\Delta E_{\Gamma=0}$ is the intrinsic resonance width of the structure without the imaginary potential.

4.5 Conclusions

In conclusion, we have investigated the role of localized imaginary potential in the scattering problems in double barrier structure. We have shown that the non-orthogonality among the eigenstates is responsible for the non-conservation of matter. We also demonstrated two applications of imaginary potential in double barrier structures. For the numerical simulation of tunneling time experiment, we have demonstrated that imaginary potential is useful to study the tunneling dynamics in the conduction band without considering the amplitude of the wavefunction in

the valence band when a recombination channel is present in the double barrier structure. For the study of asymmetric DBRT, we have discovered the tunneling without reflection in asymmetric structure with an imaginary potential which is used to model any scattering processes generally.

4.6 References

[1] A. Bohr and B. Mottelson, Nuclear Structure (Benjamin, New York, 1969), Vol. 1, pp. 430-447. See also L. D. Landau and E. M. Lifshitz, Quantum Mechanics: Non-Relativistic Theory (Pergamon, Oxford, 1977), 3rd ed., Vol. 3, p. 603.

[2] D. Pines and P. Nozières, The Theory of Quantum Liquids (Addison-Wesley, 1989).

[3] A. D. Stone and P. A. Lee, Phys. Rev. Lett. 54, 1196 (1985).

[4] S. C. Kan and A. Yariv, J. Appl. Phys. 67, 1957 (1990).

[5] A. Sa'ar, S. C. Kan and A. Yariv, J. Appl. Phys. 67, 3892 (1990).

[6] R. H. Dicke and J. P. Wittke, Introduction to Quantum Mechanics, 9th printing (Addison-Wesley, World Student Series, Reading, Massachusetts, 1980), pp. 92-93, 61.

[7] M. Tsuchiya, T. Matsusue and H. Sakaki, Phys. Rev. Lett. 59, 2356 (1987).

[8] T. B. Norris, X. J. Song, W. J. Schaff, L. F. Eastman, G. Wicks and G. A. Mourou, Appl. Phys. Lett. 54, 60 (1989).

[9] M. K. Jackson, M. B. Johnson, D. H. Chow, T. C. McGill and C. W. Nieh, Appl. Phys. Lett. 54, 552 (1989).

[10] G. Bastard and J. A. Brum, IEEE QE-22, 1625 (1986).

[11] B. Ricco and M. Ya. Azbel, Phys. Rev. B29, 1970 (1984).

[12] S. Luryi, Appl. Phys. Lett. 47, 490 (1985).

[13] T. Weil and B. Vinter, Appl. Phys. Lett. 50, 1281 (1987).

[14] M. Jonson and A. Grincwajg, Appl. Phys. Lett. 51, 1729 (1987).

[15] B. K. Ridley, Phys. Rev. B39, 5282 (1989).

[16] A. Seilmeier, H.-J. Hübner, G. Abstreiter, G. Weimann and W. Schlapp, Phys. Rev. Lett. 59, 1345 (1987).

4.7 Figures

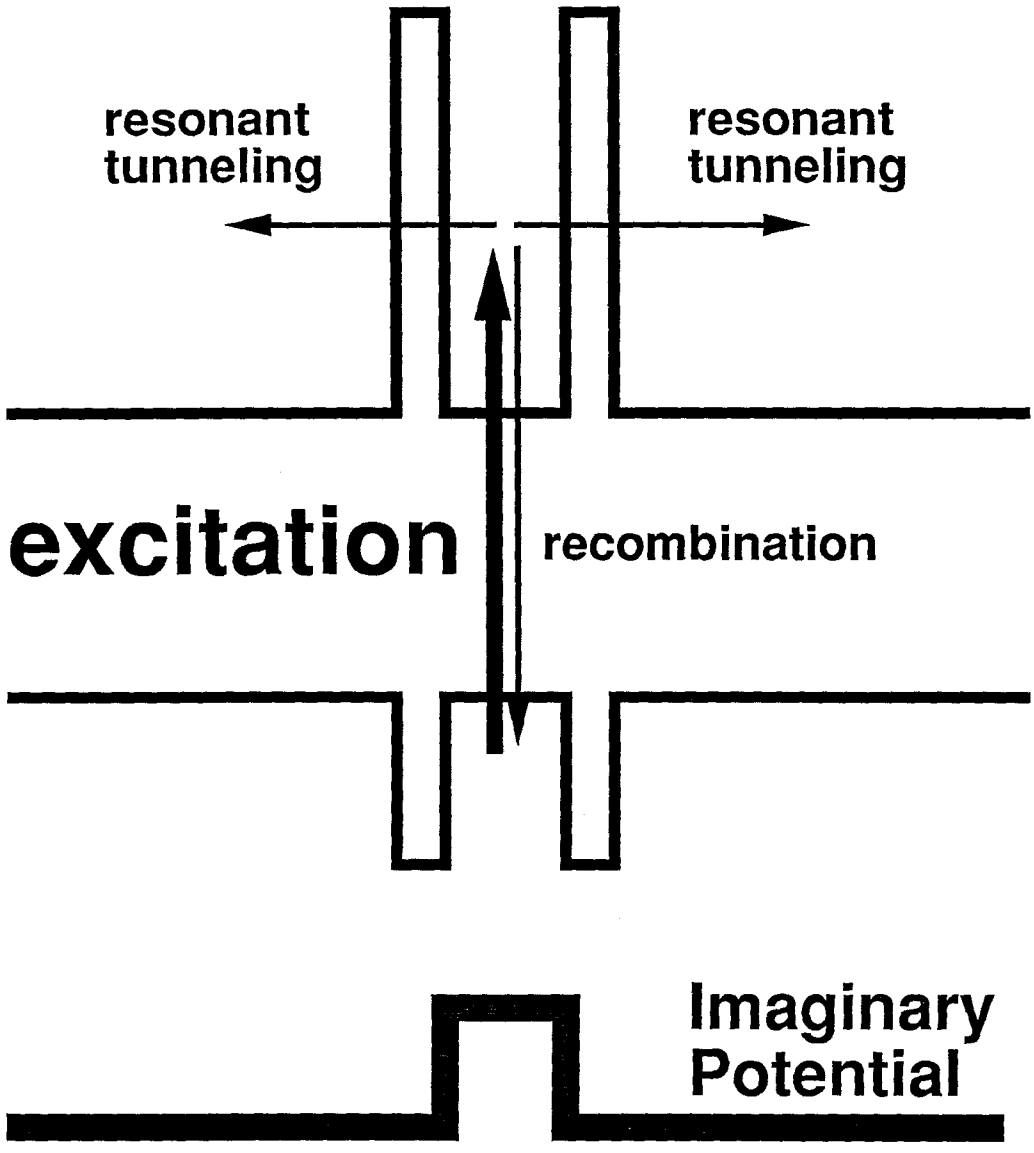

Fig. 4.1
Tunneling Time Experiment
and
Imaginary Potential

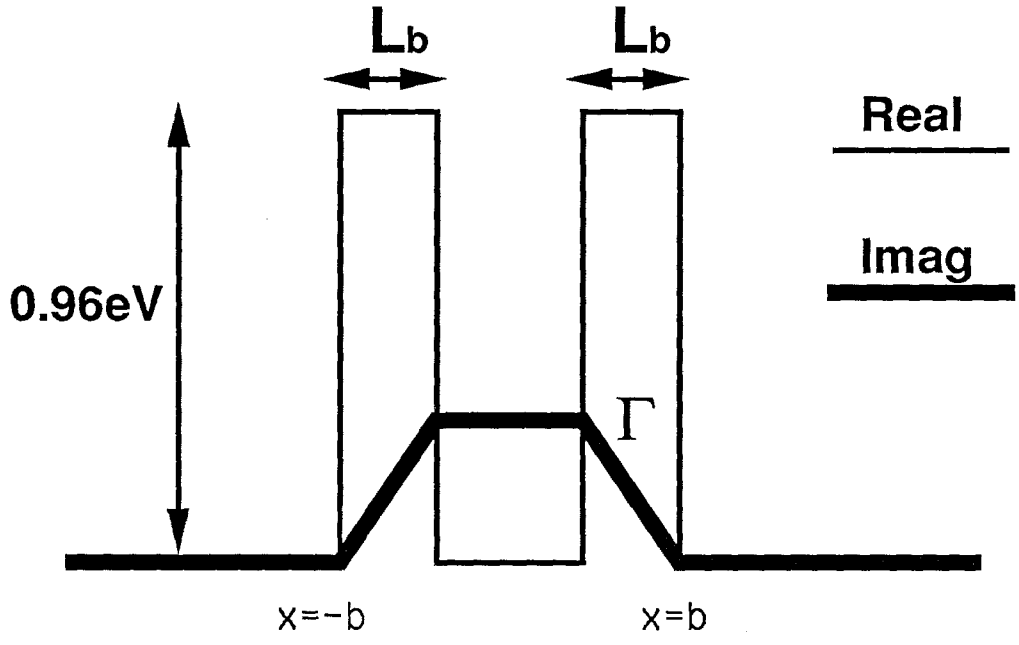

Fig. 4.2
Imaginary Potential Profile

(a) L_b = 21 Å

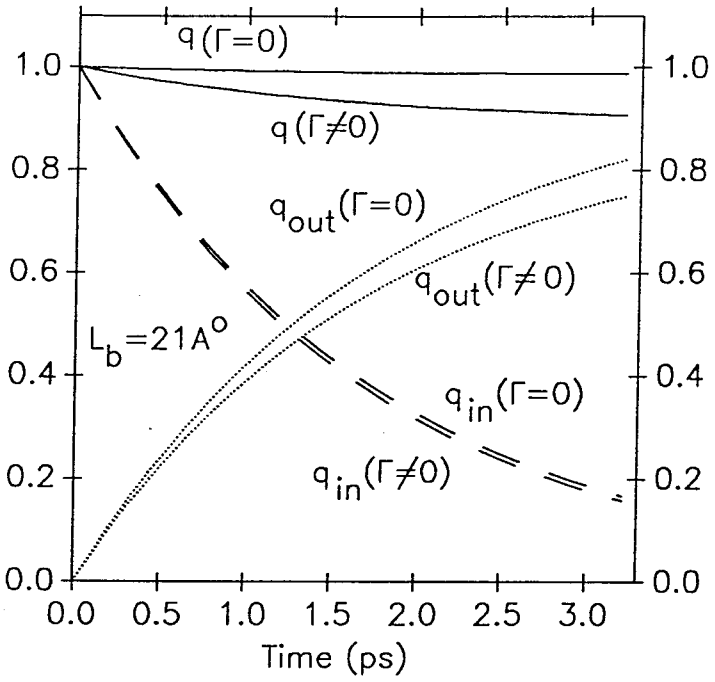

(b) L_b = 32 Å

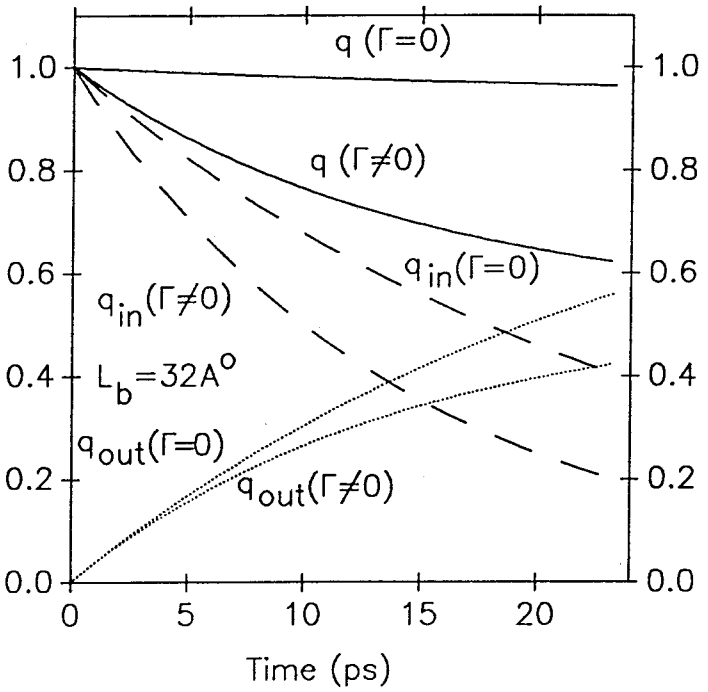

Fig. 4.3
Evolution of q(t), q_{in}(t) and q_{out}(t)

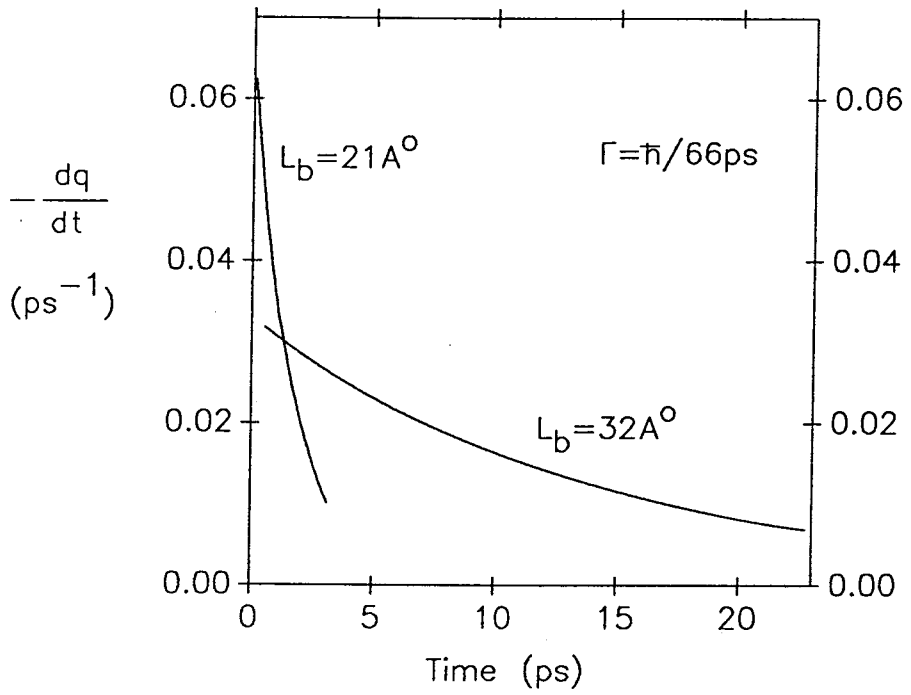

Fig. 4.4
Evolution of - dq / dt

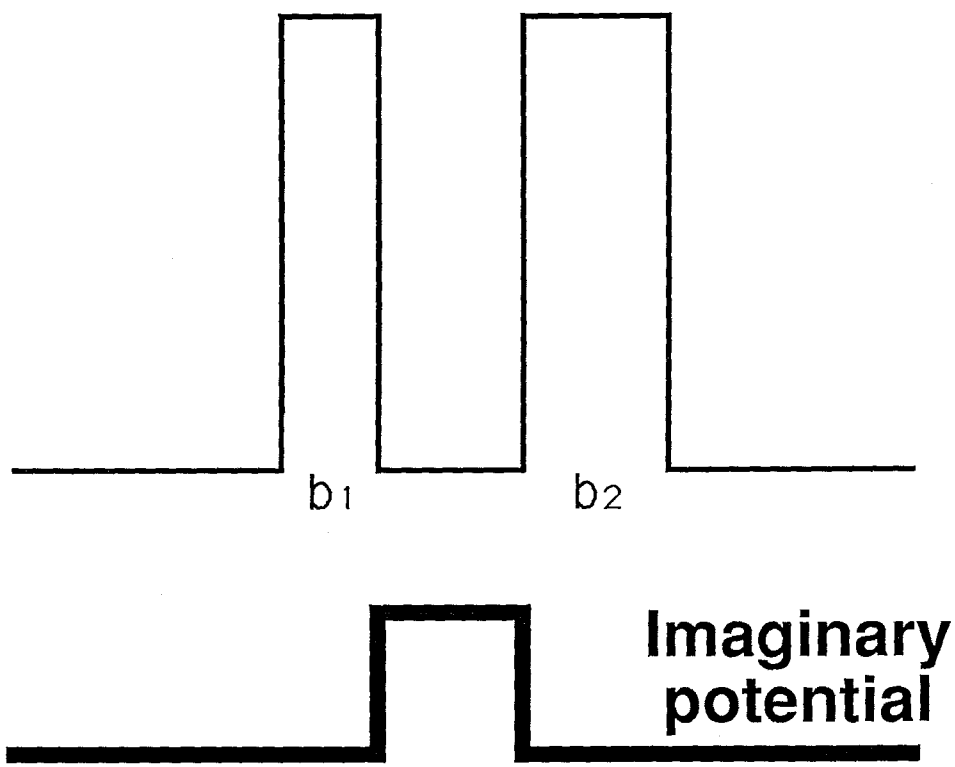

Fig. 4.5
Imaginary Potential Profile

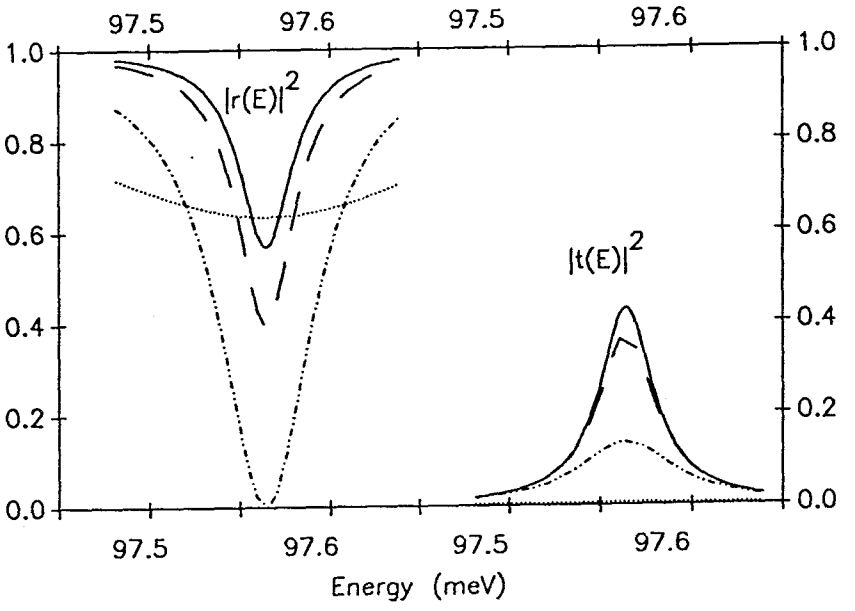

Fig. 4.6
Reflection and Transmission Spectrum of Double Barrier Structure with Imaginary Potential

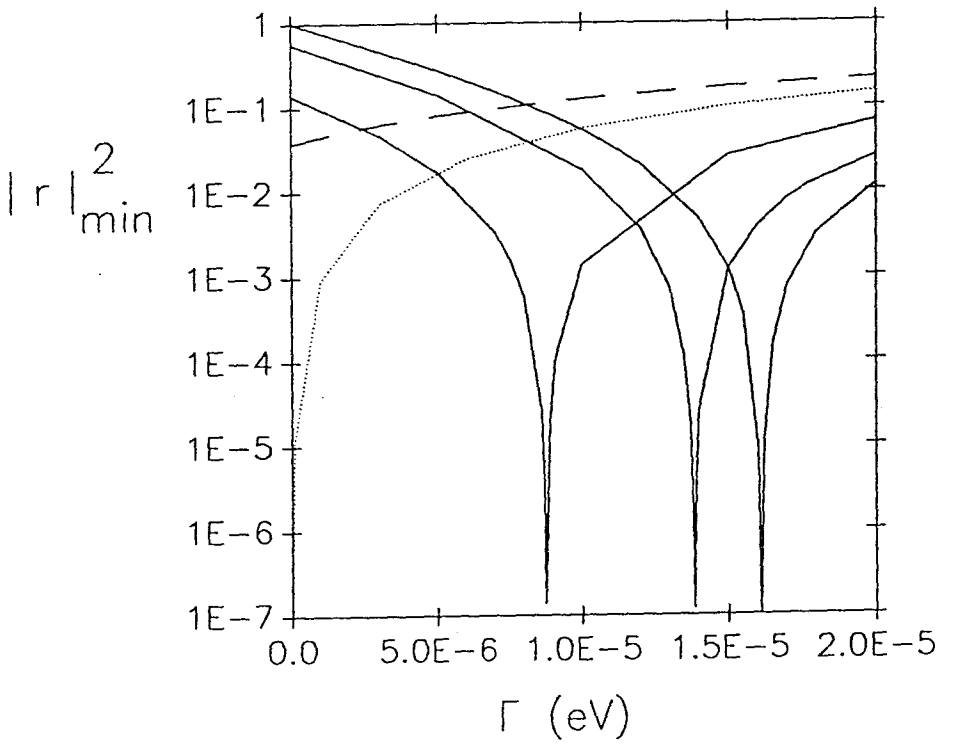

Fig. 4.7
Mininum Reflection as a function of the Magnitude of Imaginary Potential

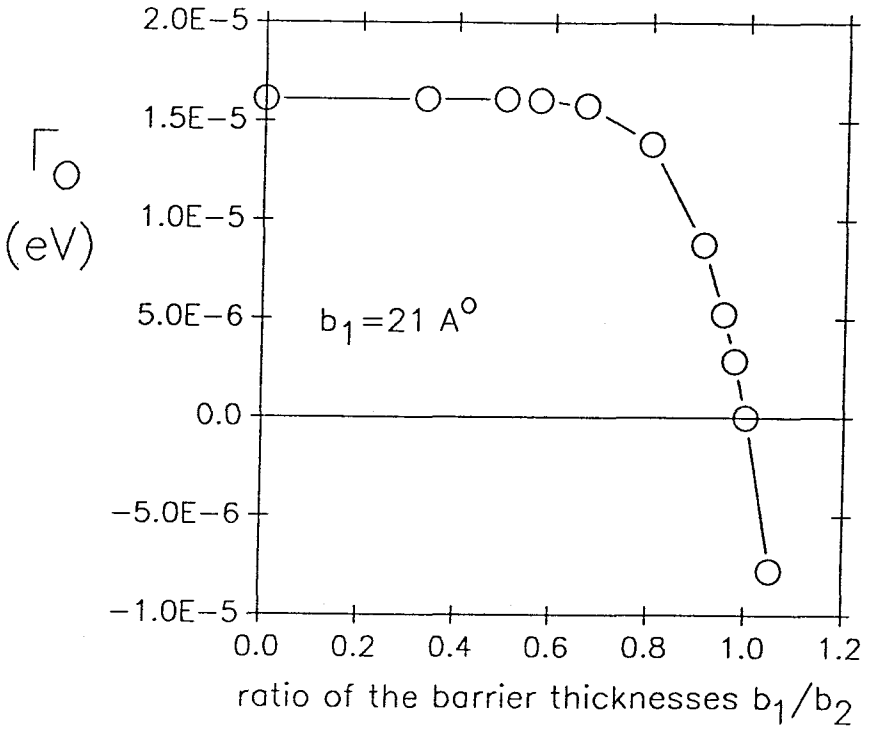

Fig. 4.8
Γ_o as a function of b_1 / b_2

Chapter Five

Optical Resonant Tunneling Devices 1a

Chapter Five

Optical Resonant Tunneling Devices

In this chapter, we introduce two optical resonant tunneling devices, Resonant Tunneling Laser (RTL) [1-2] and Optically-controlled Parallel resonant-Tunneling device (OPT) [3-5]. In recent years, DBRT structure has been used in making new electronic devices [6-12]. RTL and OPT are the first two examples of using DBRT structure in making new optical electronic devices. In RTL, the voltage-controlled resonant tunneling current is used to pump the laser diode monolithically and produce a voltage-controlled nonlinear laser output. In OPT, a new tunneling device concept called parallel resonant tunneling was developed by the author to produce several new optical electronic characteristics. RTL will be discussed in section 5.1 and OPT in section 5.2.

5.1 Resonant Tunneling Laser (RTL)

RTL is a single quantum well laser diode monolithically integrated with a DBRT structure (fig. 5.1). The single quantum well laser structure is first grown by MBE on a p-type GaAs substrate and a DBRT structure is then grown on top of the n-type top layer of the laser. The laser section includes an undoped 120 Å GaAs quantum well active region, parabolic graded index $Al_xGa_{1-x}As$ regions 3000 Å thick, with Al concentration (x) varying from 0.5 to 0.2, and cladding layers 1.7 μm thick of $Al_{0.5}Ga_{0.5}As$. The DBRT structure consists of two undoped AlAs barriers, each 20 Å thick

and an undoped quantum well, 50 Å thick. Au/AuGe and Au/AuZn metallic contacts are evaporated on the top and bottom of the device, respectively.

After the epitaxial growth, an etched mesa broad area laser of stripe width of 40 μm (fig. 5.2) is fabricated using photolithography and chemical etching. The I-V curve of the device is measured by an I-V tracer and shown in fig. 5.3. The peak and valley current density of the DBRT structure is 300A/cm^2 and 170A/cm^2 . By measuring the light output of the device as a function of the injection current, we found that the threshold current density of the laser is 250A/cm^2. The lasing wavelength was found to be 8634 Å.

5.1.1 Negative Differential Optical Response (NDOR)

The voltage-controlled laser output characteristic of the device is examined by applying a triangular voltage pulse $V_a(t)$ across the device. The circuit used in the experiment is shown in fig. 5.4. The negative of the applied voltage $-V_a(t)$, the injection current and the laser output as a function of time are shown in fig. 5.5. A resonance peak in the laser output is observed which is explained as follows. In fig. 5.6, the I-V curve of the double barrier structure and the load lines for different applied voltage ($V_a = V_{valley}$, V_{peak} and V_{high}) associated with the total series resistance to the double barrier structure are plotted. Since the resistance of the p-n junction in the laser diode is voltage-dependent, the load lines should be nonlinear. However, this nonlinearity is neglected in the following explanation. The intersection points of the I-V curve with the load lines are the operation points of the device. The x-intercept of the

load line is the applied voltage V_a across the whole device. The slope of the load line is equal to -1/R where R is the total series resistance to the double barrier structure.

In the experiment, as V_a is increased from zero, the load line moves to the right with its slope unchanged. The operation point of the device (the intersection point) , therefore, moves up from the origin along the I-V curve of the double barrier. The laser is turned on when the current is higher than the threshold current. As V_a is further increased to the resonance peak (point P) and passes V_{peak} in fig. 5.6, the operation point of the device jumps from point P to P'. Since the current at point P' is less than the threshold current of the laser, the laser is turned off. Therefore, a negative differential optical response (NDOR) is produced. As V_a is further increased so that the current is higher than threshold current, the laser is turned on again (e.g., at $V_a = V_{high}$ in fig. 5.6).

V_a is decreased at the falling edge of the triangular pulse. The laser is turned off when the current is less than the threshold current. As V_a is further decreased to the valley (point V) and passes V_{valley} in fig. 5.6, the operation point jumps from V to V'. However, since the current at V' is less than the threshold current, the laser is still off. The laser remains off to the end of the pulse.

5.1.2 Optical Memory Operation

One useful characteristic of the resonant tunneling diode is the memory property. An optical memory operation is illustrated using the Resonant Tunneling Laser. The circuit used in the experiment is shown in

fig. 5.7. The applied voltage across the device V_a and the laser output as a function of time are shown in fig. 5.8. In the beginning, V_a is increased to V_o from zero. The laser is then on because the injection current is higher than the threshold current. A positive voltage pulse is then added on the device. After the pulse, the applied voltage returns to V_o and the laser is off. A negative voltage pulse is then added on the device. After the pulse, the applied voltage returns to V_o and the laser is on again. These phenomena are explained in the following, using the concept of the load line.

In fig. 5.9, we plot the I-V curve of the double barrier structure and the load lines associated with the total series resistance to double barrier structure. Because of the negative resistance, there are three intersection points of the I-V curve with the load line for $V_a=V_o$. At which point the device will operate when $V_a=V_o$ depends on the history of V_a in the following way:

(1) If the operation point of the device moves to the point at $V_a=V_o$ from the points at $V_a > V_{peak}$ (the case after a positive pulse), then the device will operate at the point with the lowest current.

(2) If the operation point of the device moves to the point at $V_a=V_o$ from the points at $V_a < V_{valley}$ (the case after a negative pulse), then the device will operate at the point with the highest current.

Since the device will operate at the point even after the input pulse passes away, the device exhibits a memory operation.

5.2 Optically-controlled Parallel resonant-Tunneling (OPT)

In this section, we introduce another new optical resonant tunneling device called OPT which stands for Optically-controlled Parallel resonant-Tunneling. A completely new resonant tunneling concept (Parallel resonant-Tunneling) was developed in this new device to produce several new optical electronic characteristics:

(1) a negative photoconductivity,

(2) a new bistable photoconductivity (positive and negative),

(3) a new middle trace, and

(4) the optical switching of the new middle trace.

In section 5.2.1, the OPT structure will be introduced. In section 5.2.2, the experimental result will be presented. In section 5.2.3, a theory of the middle trace and its optical switching will be described.

5.2.1 OPT Structure

The OPT structure, which is shown in fig. 5.10, consists of a double barrier resonant tunneling structure grown by MBE on an n-type GaAs substrate: two 40 Å undoped AlAs barrier layers and a 47 Å undoped GaAs quantum well layer. A 7000 Å n-type GaAs layer is grown on top of the double barrier structure. The mesa structure shown in fig. 5.10 consists of a top surface of 100 μm x 25 μm, capped by a AuGe/Au contact, is 0.1 μm high and is sitting atop a 100 μm x 75 μm base. The back side of the substrate is coated with another AuGe/Au contact. The mesa structure was fabricated by conventional photolithographic techniques and wet

etching. In the experiment, a voltage V_a is applied across the two metal contacts.

The main characteristic of OPT device which is different from the traditional resonant tunneling devices is that the voltage drop across the double barrier structure:

$$V(x) \equiv \phi(x\ ,\ y=y_{top}) - \phi(x\ ,\ y=y_{bottom})\ ,$$

where $\phi(x\ ,\ y)$ is the electrical potential inside the device, $y = y_{top}$ and $y = y_{bottom}$ are shown in fig. 5.11, varies laterally along the structure in the x-direction while it is constant in traditional devices as shown in fig. 5.11. The variation of V(x) does not exist in the traditional devices because the electric field is perpendicular to the double barrier structure. Due to the variation of V(x) in OPT, the resonant tunneling processes along the tunneling plane in x-direction do not occur everywhere simultaneously.

A circuit model shown in fig. 5.12 is developed to study the tunneling processes in OPT. It consists of an array of resonant tunneling diodes T_i $(1 \le i \le N)$, each simulating the resonant tunneling process on part of the tunneling plane. The array is connected to a resistor network (determined by the resistors, R_1, R_2, R_m and R_3) which simulates the top layer of the device. A voltage V_a is applied across the terminals of the circuit. The total tunneling current (I_{total}) can be written as the sum of the diode current (I_i) which depends on the diode voltage (V_i):

$$I_{total} = \sum_{i=1}^{N} I_i(V_i)$$

or, in the continuous case, the sum becomes an integral:

$$\int_0^L J[x,V(x)]\ dx$$

where L is the length of the device in x-direction and J[x,V(x)] is the current density at point x which depends on V(x). Therefore, the total current is a functional of V(x) or { V_i (i=1 to N) }. In a traditional device, V(x) is equal to a constant which depends on the applied voltage V_a and therefore, the total current is only a function of V_a.

5.2.2 Operation Principle of OPT

As discussed above, the total current of the device depends on the variation of V(x). When V(x) = constant, all the diodes in the circuit model can reach the resonance state at the same applied voltage V_a. Therefore, the peak current of the device $I^p_{total} = N\, I^p_i$ and the valley current of the device $I^v_{total} = N\, I^v_i$ where I^p_i and I^v_i are the peak and valley current of the individual diode, respectively. When V(x) $\neq$ constant, each diode reaches the resonance state at a different applied voltage V_a. Therefore, $I^p_{total} < N\, I^p_i$ and $I^v_{total} > N\, I^v_i$ as shown in fig. 5.13. The difference between I^p_{total} and $N\, I^p_i$ (or, I^v_{total} and $N\, I^v_i$) increases with the variation of V(x). Therefore, we can increase and decrease the peak and valley current, respectively, by decreasing the variation of V(x).

Now, we consider the dependence of V(x) on the top layer's conductivity of the device. V(x) is constant if the top layer's conductivity is infinite. When the top layer's conductivity is finite, the electric field has a non-zero component in x-direction because of the device geometry. Therefore, V(x) is not constant. The amount of the variation of V(x) decreases with the top layer's conductivity. In the experiment, we increase the conductivity by illuminating the top layer with light. The

variation of V(x) will then decrease and the resonant tunneling peak will become sharper.

The measured I-V curve of the device is determined by the intersection points of the load line with the intrinsic I-V curve of the device. When the load line is moved into the region shown in fig. 5.14 (as the case for the optical memory in section 5.1.2), there are two stable points at which the device can operate. When the device is illuminated with light, the peak current will increase and the valley current will decrease in the intrinsic I-V curve as discussed above. The stable point with higher current thus moves up while the stable point with lower current moves down as shown in fig. 5.14. The decrease of the current at the lower stable point demonstrates the negative photoconductivity. The optical effect on both the high and low current states demonstrates a new bistable photoconductivity (positive and negative).

5.2.3 Experimental Results

The current-voltage (I-V) characteristics of OPT are measured by an I-V tracer at room temperature and shown in fig. 5.15. The lower left I-V curve is measured when the device is not illuminated. A resonant peak is observed. The lower right I-V curve is measured when the device surface is illuminated by a tungsten lamp of 500 W/cm^2. We found that the peak current is increased by 4 mA and the valley current is decreased by 24 mA.

The upper left and right I-V curves are measured with the maximum applied voltage on the device increased by 0.2 volt. The upper left I-V

curve is measured when the device is not illuminated. A third trace appears after the second trace in the lower left I-V curve. The upper right I-V curve is measured when the device is illuminated. The second trace on the upper left I-V curve disappears. In the following, we call the three traces shown in the upper left I-V curve as the peak trace, the middle trace, and the valley trace, respectively. The upper two I-V curves show the middle trace can be switched off optically. The lower two I-V curves show the optical switching from the middle trace to the valley trace. The changes of the peak and valley traces with light (the peak current is increased by 4 mA and the valley current is decreased by 3 mA) also show the demonstration of the positive and negative photoconductivities explained above.

5.2.4 Theory of the Middle Trace

In order to understand the new middle trace observed in the experiment, we calculate the I-V curve of the circuit model shown in fig. 5.12. The result is shown in fig. 5.16. The middle trace observed in the experiment is reproduced from the calculation. The origin of the middle trace involves new tunneling dynamics discovered in OPT which will be described in the following. The optical switching of the new middle trace can also be explained.

Our circuit model consists of an array of resonant tunneling diodes, T_i ($1 \leq i \leq 101$), which are all grounded at the bottom contact plane. The top side of each T_i is connected to the applied voltage V_a through a resistor network which simulates the top layer of the device. The voltage across

each T_i is V_i. The I-V characteristic of each T_i is modeled by two linear branches (peak branch and valley branch) shown in fig. 5.17.

On the peak branch, where $V_i < V_p$,

$$I_i = V_i / R_p \ ;$$

on the valley branch, where $V_i > V_p$,

$$I_i = I_v + (V_i - V_p) / R_v$$

where V_p is the voltage at the resonance peak, R_p and R_v are the resistance of the peak branch and valley branch, respectively, and I_v is the valley current. The first diode (T_1) simulates the part of tunneling plane (25 μm x 100 μm) under the metal contact, while the other T_i's ($2 \leq i \leq 101$) simulate the rest of the tunneling plane (each for an area of 0.5 μm x 100 μm). R_1 , R_2 and R_m are estimated using the resistance formula, $R=L/\sigma A$. σ is taken to be $1.0 \times 10^5\ \Omega^{-1}\ m^{-1}$. $R_1 = 0.05\Omega$. $R_2 = 0.2\Omega$. $R_m=R_2/50$. $R_3=2R_1$. $V_p=0.2V$. $R_p=10^{-4}\ \Omega\ cm^2$. Therefore, $I_p=2\ kA/cm^2$. I_v is taken to be $0.6\ kA/cm^2$.

In order to understand the origin of the middle trace, we follow the change of V_i's on each diode when the applied voltage, V_a , is increased from zero to V_{final} in the following:

STAGE ONE (Peak trace) --- When V_a is increased from zero, I_{total} grows linearly with V_a as all the diodes are still on the peak branch until one of V_i's reaches V_p. Since the effective resistance between the top metal contact and the diode (T_i) increases with i, V_i always decreases with increasing i. As V_1 is the largest V_i, switching first occurs when V_1 equals V_p. This switching causes discontinuous changes over all node voltages. Other diodes T_j's ($j > 1$) may also switch to the valley branch if their final

V_j's after this discontinuous change are greater than V_p. However, at this switching, only the first diode switches to the valley branch. All other diodes stay at the peak branch because the discontinuous increase of V_j due to the switching is not large enough to bring T_j to the valley branch. We called it a one-diode change. This is the first large discontinuity shown in fig. 5.16.

STAGE TWO (Middle trace) --- As V_a increases further, the change of each V_i is continuous until V_2 equals V_p. The switching of T_2 to the valley branch introduces a discontinuous increase in all the node voltages and only diode T_2 switches to the valley branch, i.e., another one-diode change. Similar one-diode changes occur successively for the diode from T_3 to T_{68} as V_a increases, until V_{69} equals V_p. However, the change of I_{total} caused by all these one-diode changes from T_2 to T_{68} is very small because these diodes are much smaller than the first diode (1:50). These small changes are not resolvable in fig. 5.16 but the locus of (V_a, I_{total}) forms a middle trace.

STAGE THREE (Valley trace) --- When T_{69} switches to the valley branch, all the diodes which are still on the peak branch (T_{70} - T_{101}) switch to the valley branch because those V_i's (V_{70} - V_{101}) after the change are larger than V_p. This is the second large discontinuity shown in fig. 5.16. Further increase of V_a does not cause any additional discontinuous change of the V_i's.

The switching dynamics in the backward scan of V_a from V_{final} to zero are qualitatively the same as the dynamics in the forward scan of V_a.

The number of diodes in the many-diode change at the right-hand side of the circuit and the values of V_a at the discontinuous changes are different, resulting in the hysteresis shown in fig. 5.16.

The experimental result in fig. 5.15 also shows the optical switching of the middle trace: it disappears when the device surface is illuminated. Since the illumination is to increase the top layer's conductivity σ, we increase σ from $1.0 \times 10^5\ \Omega^{-1}\ m^{-1}$ to $1.3 \times 10^5\ \Omega^{-1}\ m^{-1}$ in our model and reduce R_1, R_2, R_m and R_3 accordingly to simulate the optical effect. The calculated I-V curve for the circuit with $\sigma = 1.3 \times 10^5\ \Omega^{-1}\ m^{-1}$ is shown by the curve on the right in fig. 5.16. Compared to the I-V curve on the left, the middle trace for $\sigma = 1.3 \times 10^5\ \Omega^{-1}\ m^{-1}$ occurs for a smaller range of V_a, and its slope decreases. The optical switching of the middle trace in the experiment can now be explained by considering the attainable points on the intrinsic I-V characteristic. The measured I-V characteristic that we actually observe consists of the intersection points of the load line with the intrinsic I-V characteristic of the device shown in fig. 5.16. When the device is not illuminated, the middle trace intersects the load line and, therefore, can be observed. However, under illumination, the top layer's conductivity increases, eliminating the intersection point of the middle trace with the load line as shown in fig. 5.16, so the middle trace is not seen. Fig. 5.16 also shows the positive and negative photoconductivities explained and observed above.

5.3 Conclusions

In conclusion, we have demonstrated the first series of resonant tunneling devices (RTL and OPT). We have observed the basic optical resonant tunneling characteristics in RTL and demonstrated the optical memory operation. We have developed an optically-controlled parallel resonant tunneling process in OPT and observed the negative photoconductivity, a bistable photoconductivity (positive and negative), a new middle trace and its optical switching.

5.4 References

[1] I. Grave', S. C. Kan, G. Griffel, S. Wu, A. Sa'ar and A. Yariv, "A Monolithic Integration of a Resonant Tunneling Diode and a Quantum Well Semiconductor Laser," 1990 Conference on Lasers and Electro-Optics (CLEO), 21-25 May, Anaheim, California, Paper CPDP28, p. 595.

[2] I. Grave', S. C. Kan, G. Griffel, S. Wu, A. Sa'ar and A. Yariv, Appl. Phys. Lett. 58, 110 (1991).

[3] S. C. Kan, S. Wu, S. Sanders, G. Griffel, and A. Yariv, Annual Meeting of Optical Society of America, 4-9 November 1990, Paper TuA2.

[4] S. C. Kan, S. Wu, S. Sanders, G. Griffel, and A. Yariv, J. Appl. Phys. 69, 3384 (1991).

[5] S. C. Kan, S. Sanders, G. Griffel, G. H. Lang, S. Wu, and A. Yariv, Appl. Phys. Lett. 58, 1548 (1991).

[6] L. L. Chang, L. Esaki and R. Tsu, Appl. Phys. Lett. 24, 593 (1974).

[7] F. Capasso and R. A. Kiehl, J. Appl. Phys. 58, 1366 (1985).

[8] A. R. Bonnefoi, D. H. Chow and T. C. McGill, Appl. Phys. Lett. 47, 888 (1985).

[9] N. Yokoyama, K. Imamura, S. Muto, S. Hiyamizu, and H. Nishi, Japanese J. Appl. Phys. 24, L854 (1985).

[10] A. R. Bonnefoi, T. C. McGill, and R. D. Burnham, IEEE EDL-6, 636 (1985).

[11] F. Capasso, S. Sen, and A. Y. Cho, Appl. Phys. Lett. 51, 526 (1987).

[12] F. Capasso, S. Sen, A. Y. Cho, and D. L. Sivco, Appl. Phys. Lett. 53, 1056 (1988).

5.5 Figures

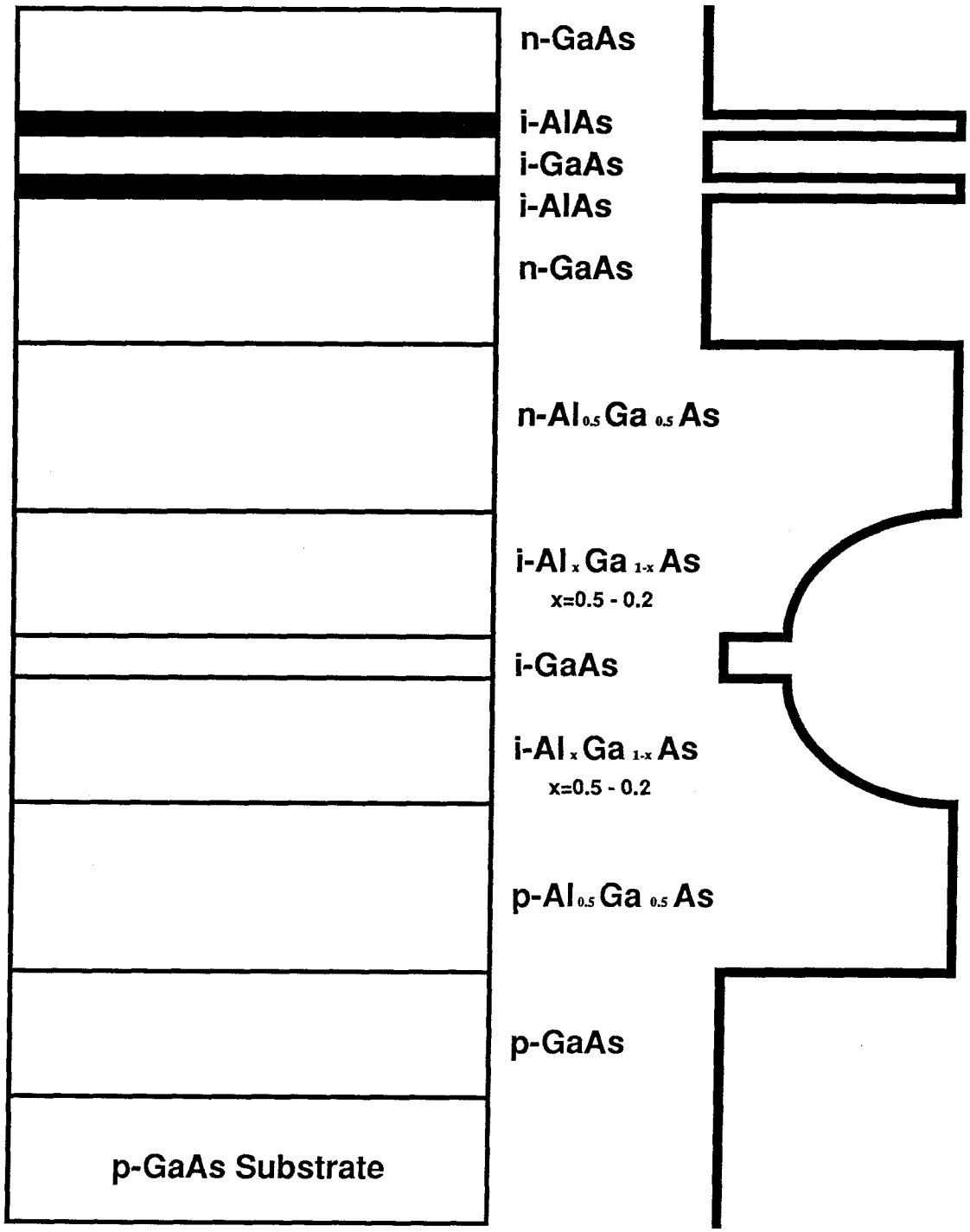

Fig. 5.1
Resonant Tunneling Laser Structure

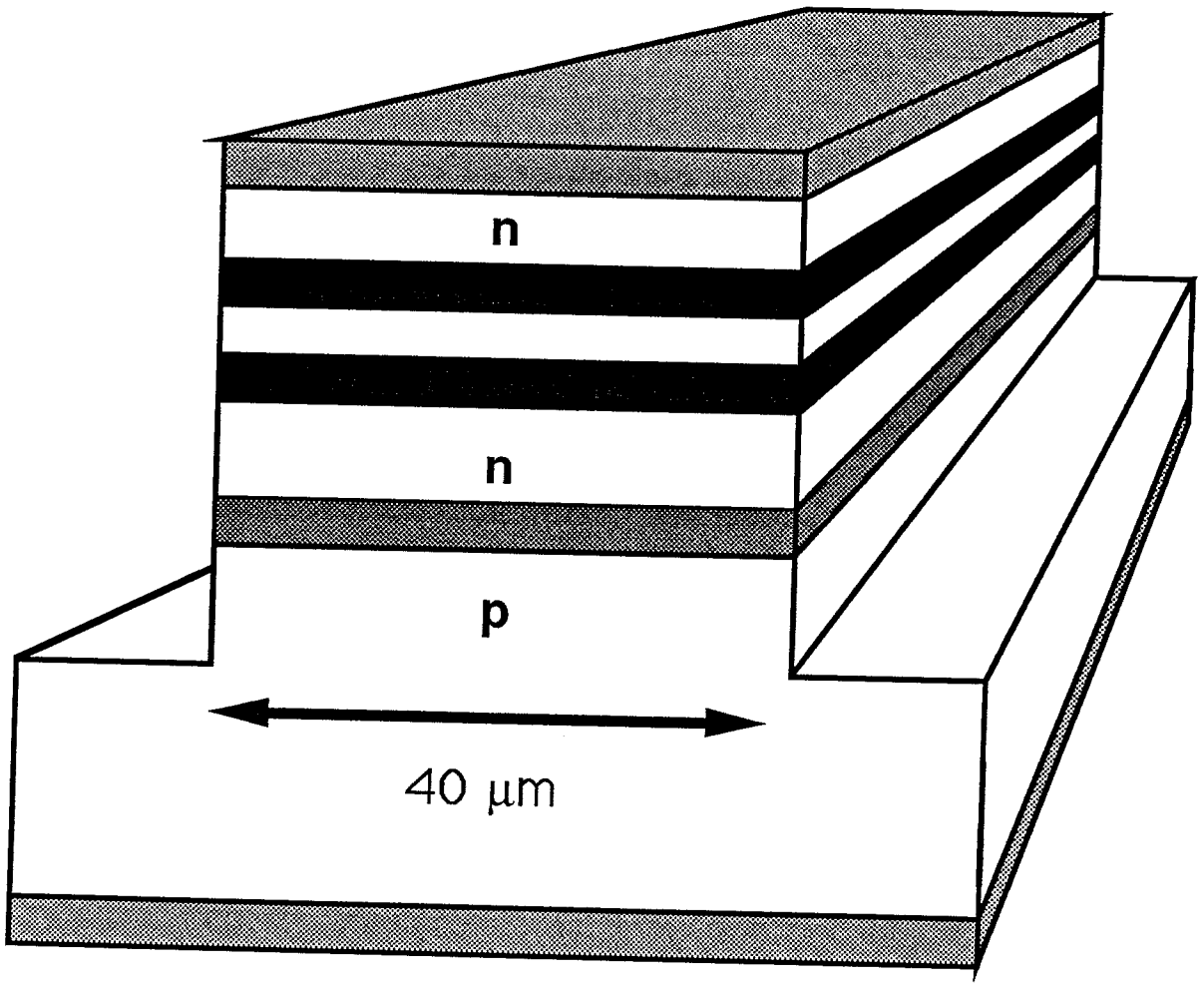

Fig. 5.2
Broad Area Laser Structure

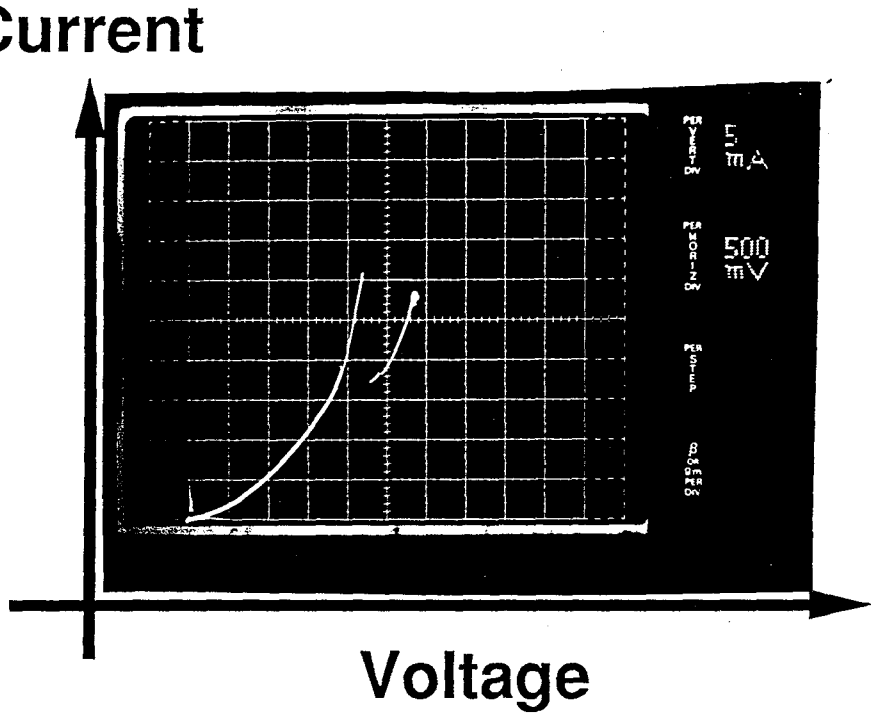

Fig. 5.3
I-V curve of RTL

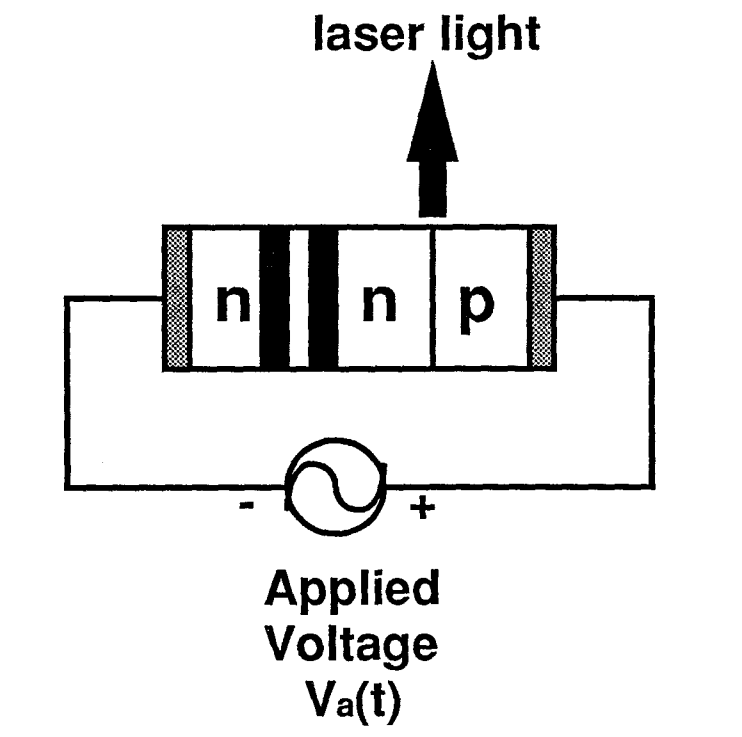

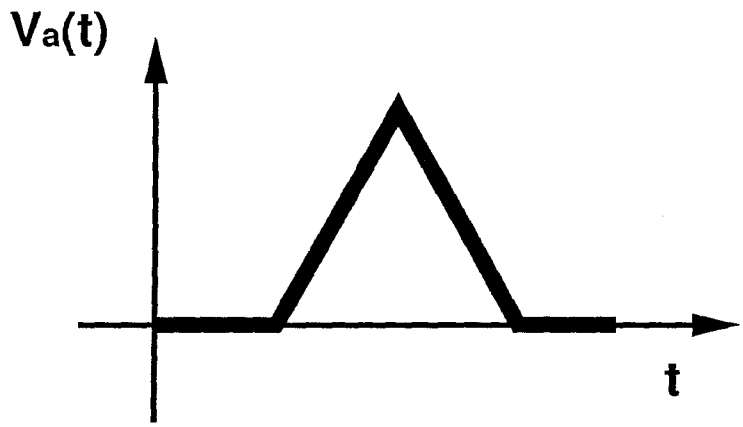

Fig. 5.4
Applied Voltage Profile

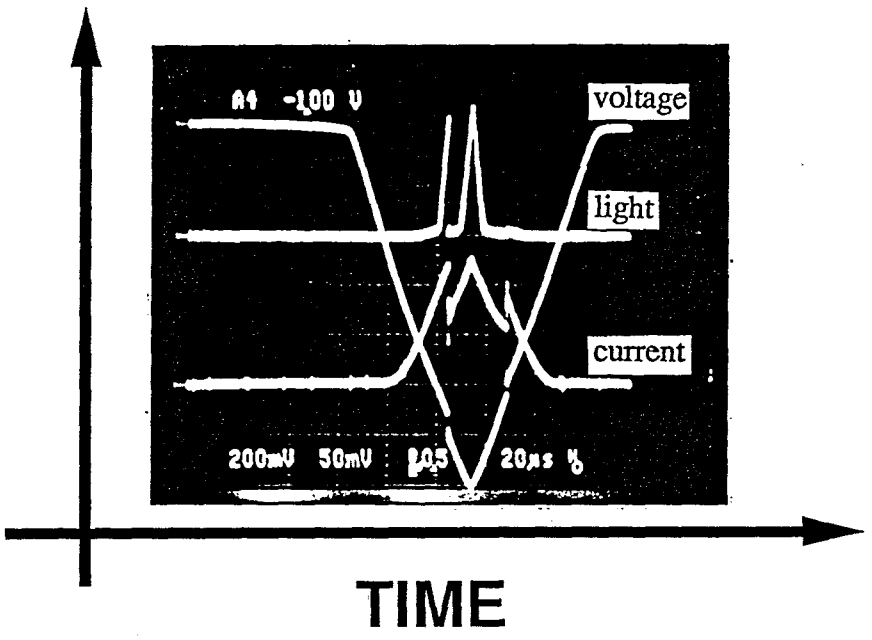

Fig. 5.5
Experimental Results

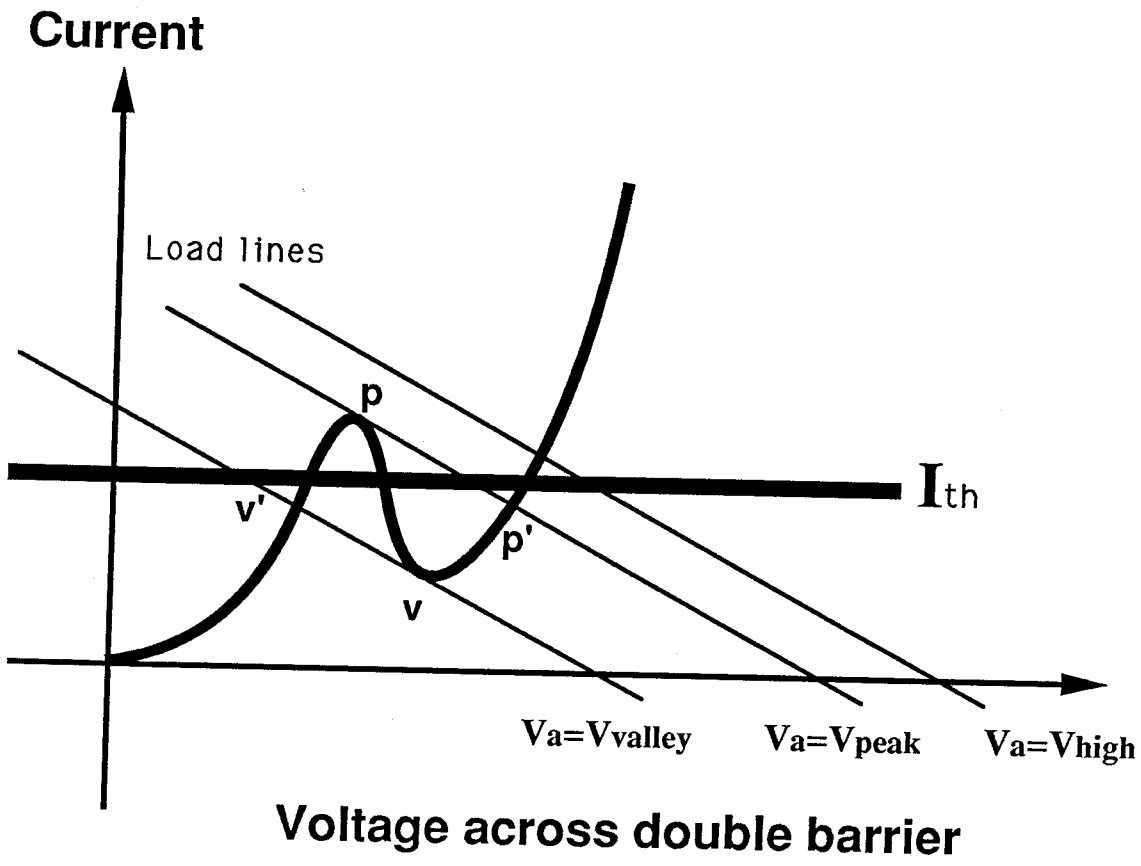

Fig. 5.6
Explanation of Experimental Result

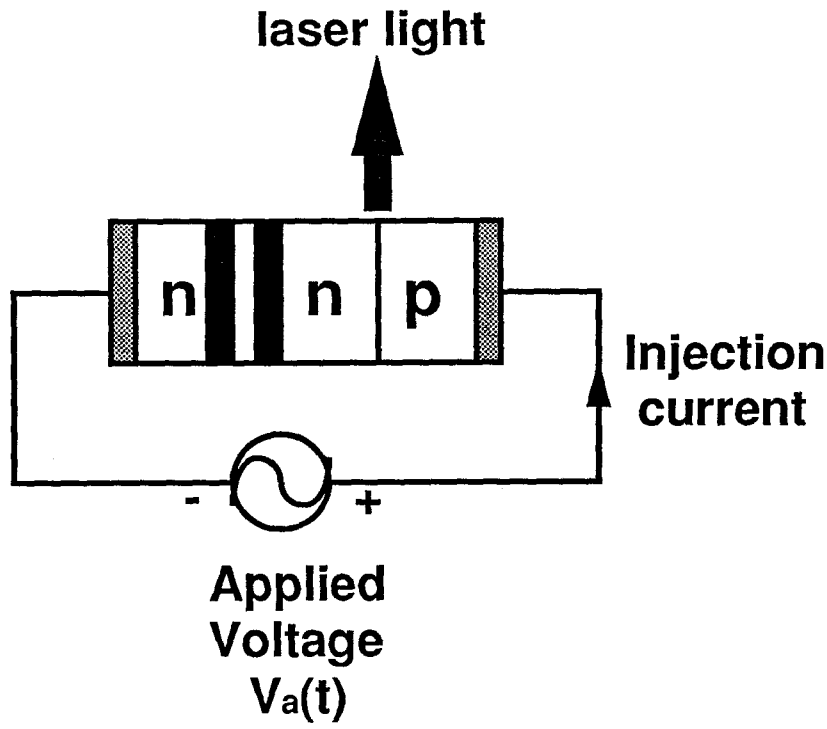

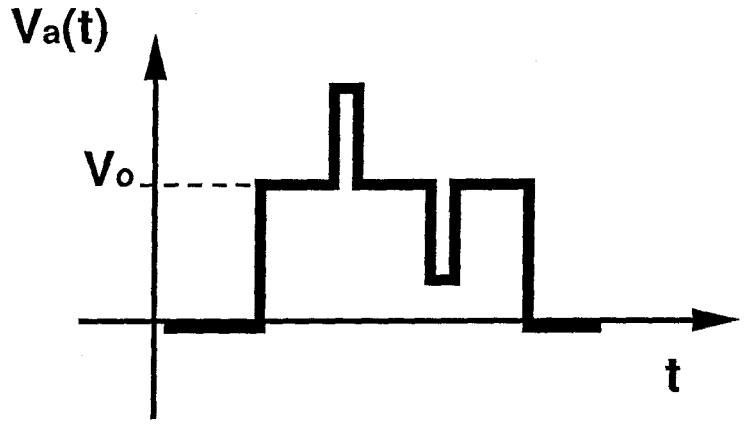

Fig. 5.7
Applied Voltage Profile

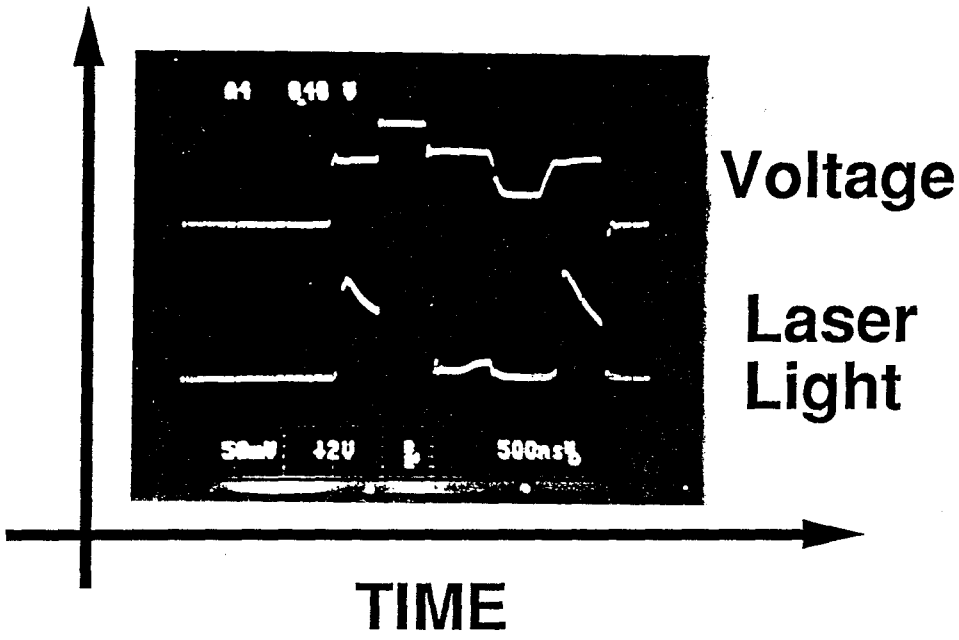

Fig. 5.8
Memory Operation of RTL

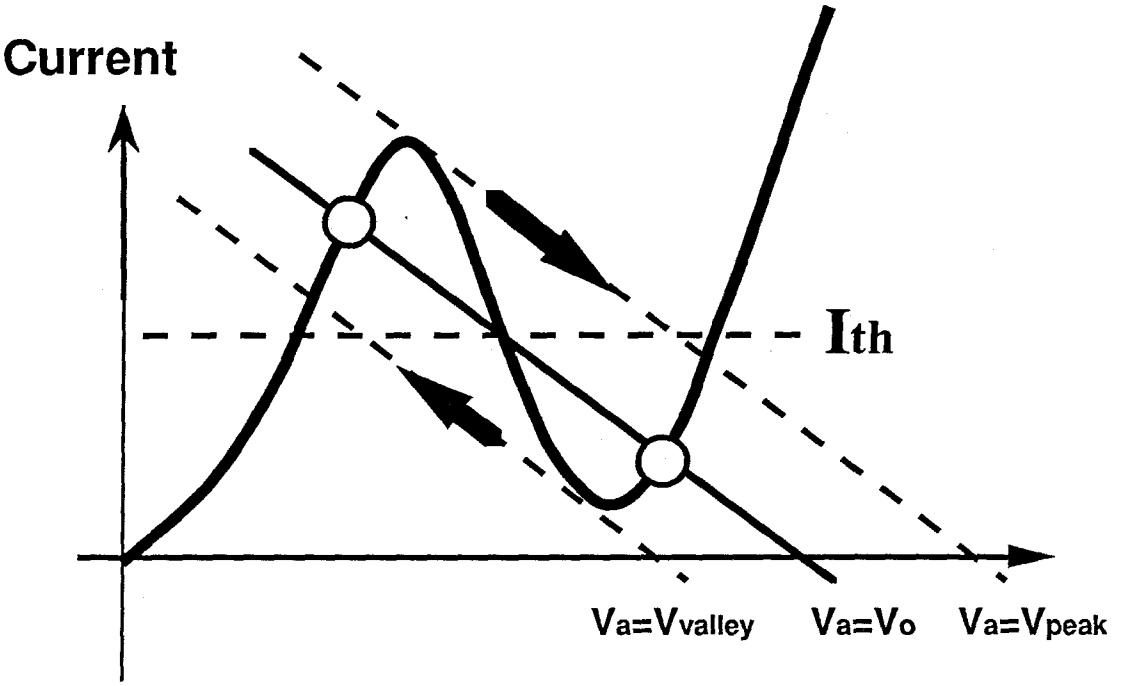

From below -- high current
From above -- low current

Fig. 5.9
Explanation of RTL Memory Operation

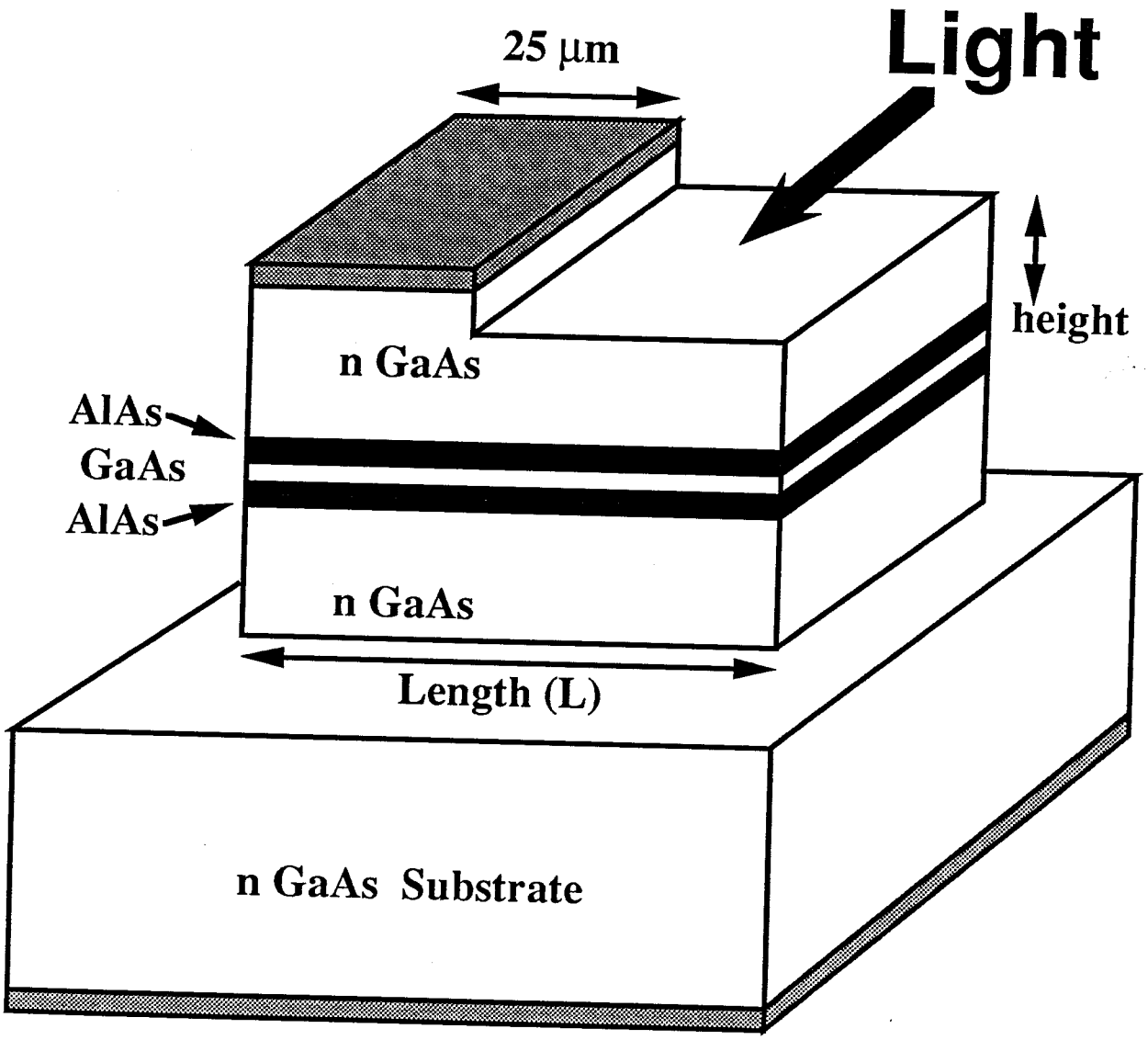

Fig. 5.10
OPT Structure

OPT

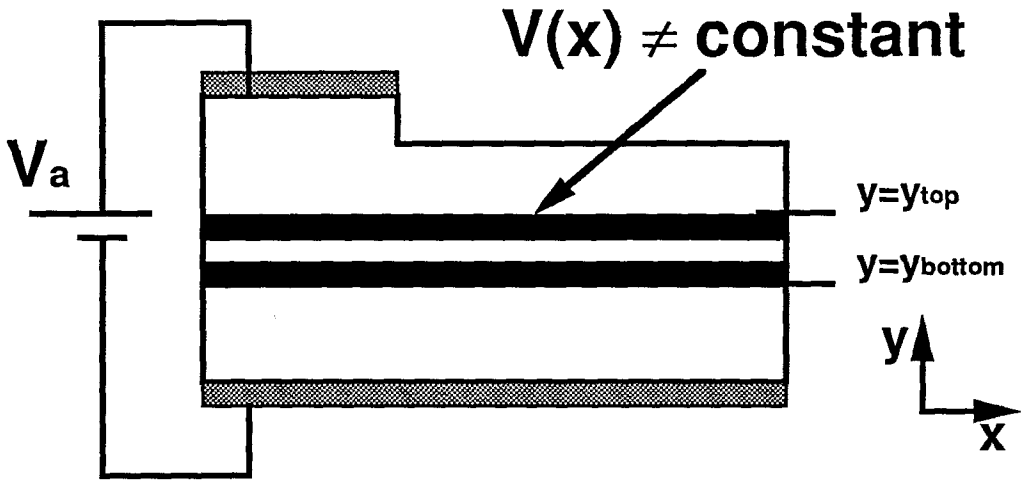

Traditional Device

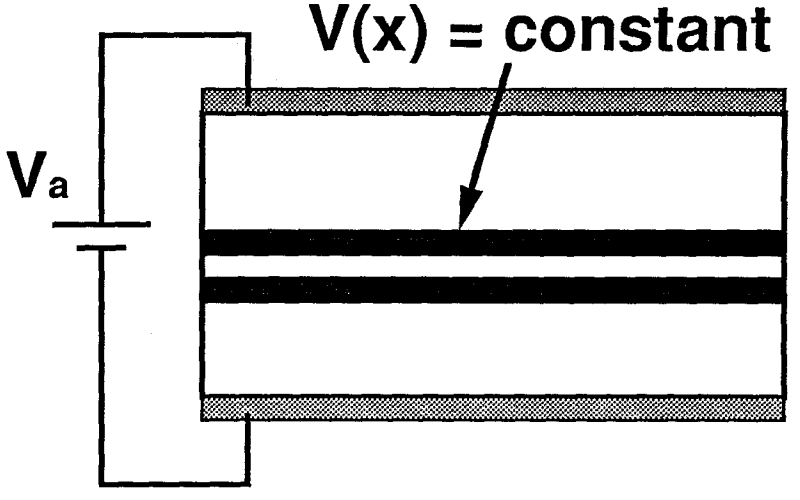

Fig. 5.11
Difference between
OPT and Traditional Device

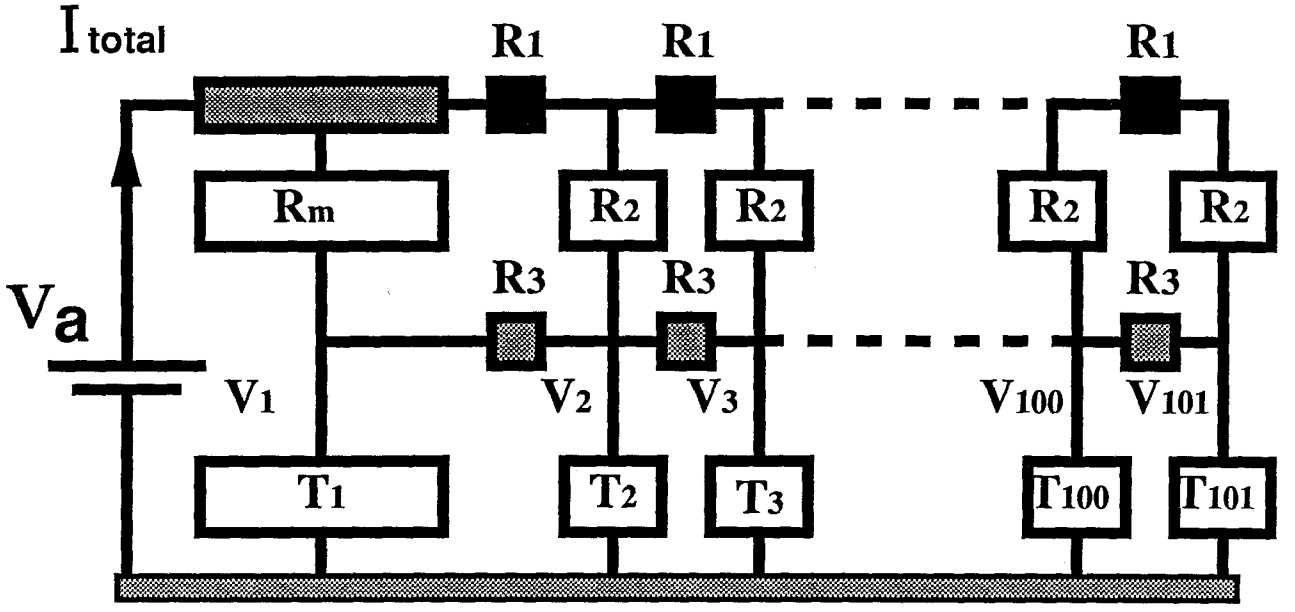

Fig. 5.12
Circuit Model of OPT

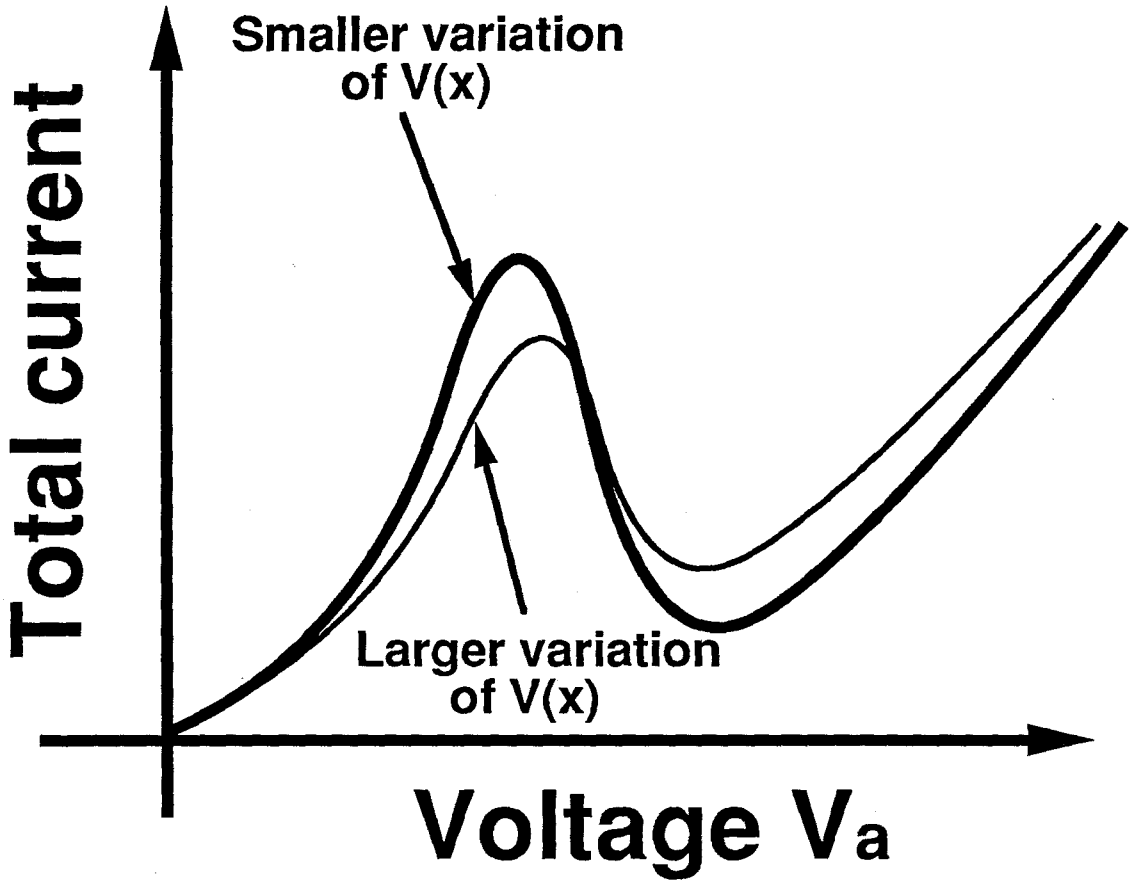

Fig. 5.13
Change of Resonant Peak

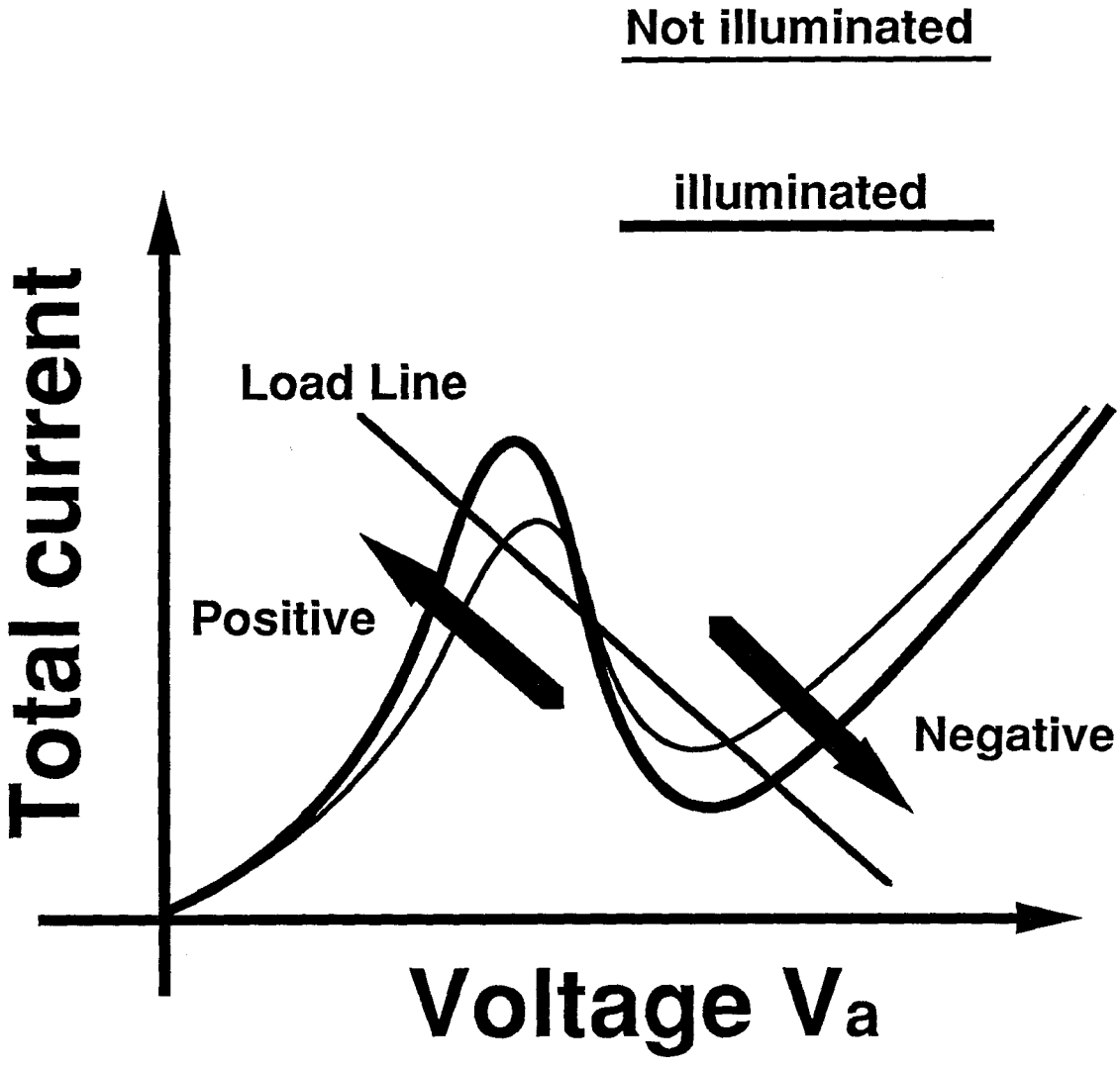

Fig. 5.14
Optical Effect on OPT

Light off
$V_{max}=V_{large}$

Light on
$V_{max}=V_{large}$

Light off
$V_{max}=V_{small}$

Light on
$V_{max}=V_{small}$

Fig. 5.15
Experimental I-V Curves of OPT

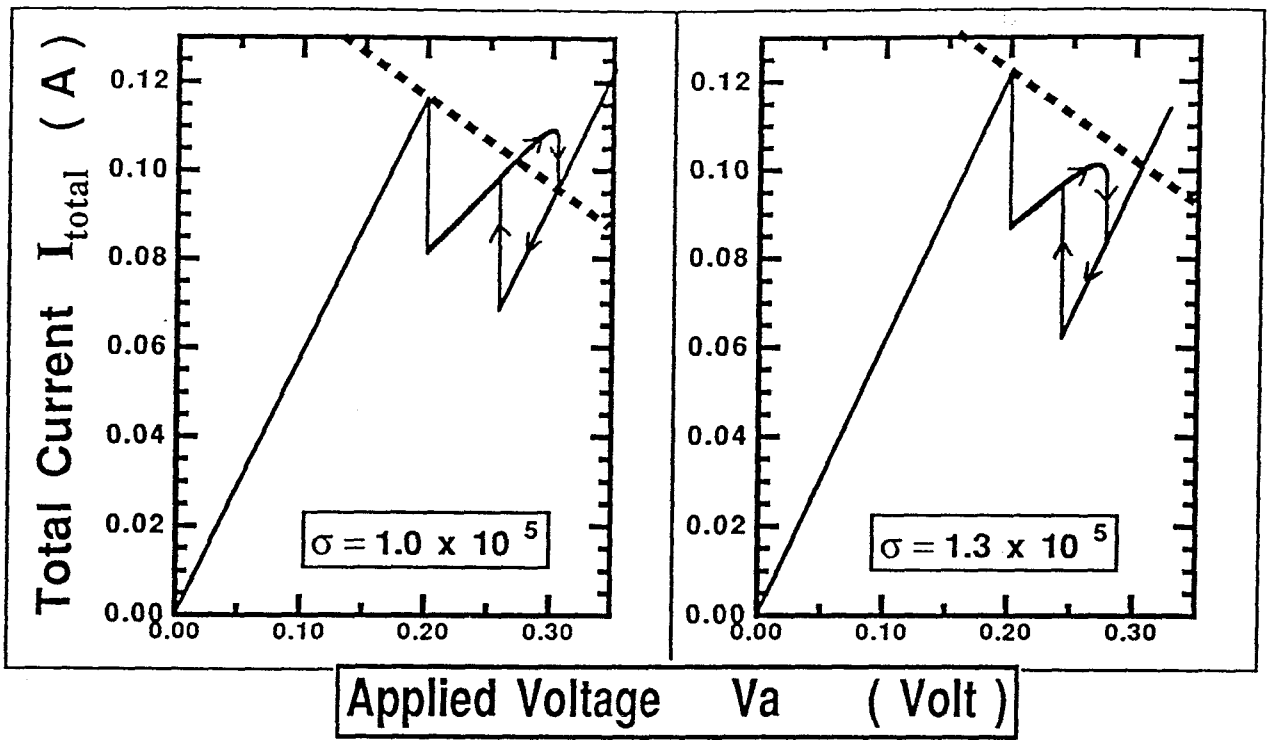

Fig. 5.16
Middle Trace and Optical Switching

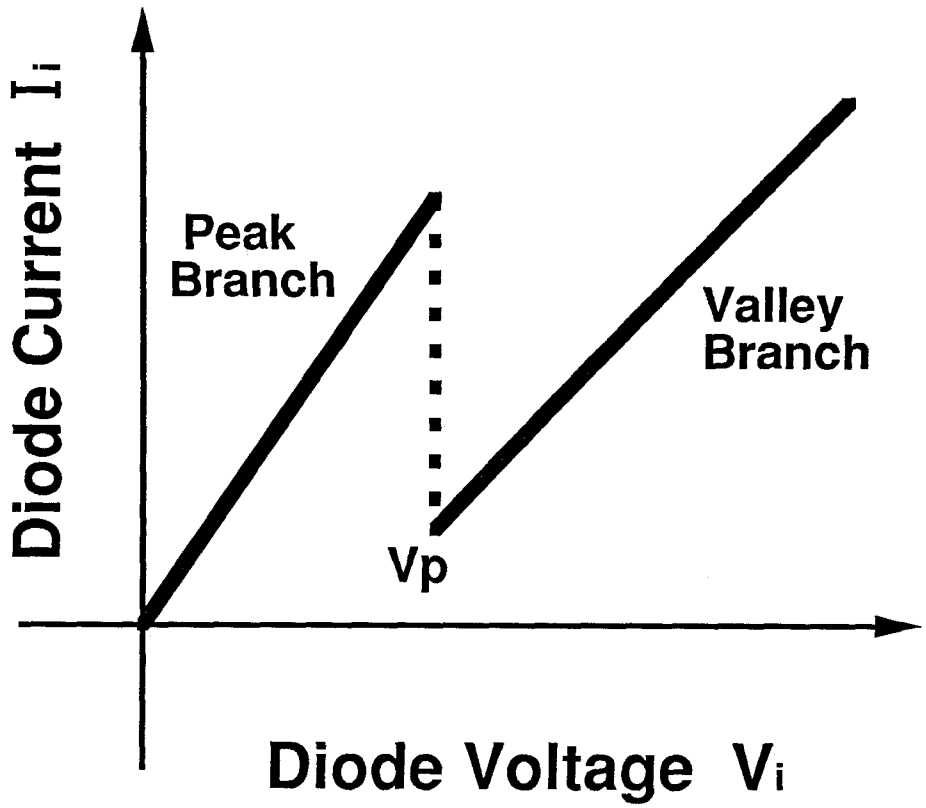

Fig. 5.17
I-V Curve of Individual Diode in the Ciruit Model of OPT

Appendix

Crank-Nicolson Scheme for Simulation of Tera Hertz DBRT

A 1 Explicit and Implicit Schemes

Simulation of the evolution of an electronic wavefunction in a double barrier structure modulated in time is done by solving the time-dependent Schrödinger equation:

$$\hbar\, i \frac{\partial \Psi(z,t)}{\partial t} = -\frac{\hbar^2}{2m^*} \frac{\partial^2 \Psi(z,t)}{\partial z^2} + V(z,t)\, \Psi(z,t) \qquad \text{(A1)}$$

where $\hbar = h/2\pi$ and h is Planck's constant, $\Psi(z,t)$ is the electron wavefunction, m* is the effective mass and V(z,t) is the modulated double barrier potential. Since the Schrödinger equation is a parabolic partial differential equation with a first order derivative of $\Psi(z,t)$ with respect to time, $\Psi(z,t)$ can be found when the initial $\Psi(z,t_o)$ at $t = t_o$ is given. A straightforward numerical method called explicit scheme is described as follows. Equation (A1) can be rewritten as:

$$\hbar i\, \partial\Psi/\partial t = H\Psi \qquad \text{(A2)}$$

where H is the Hamiltonian operator. In the numerical method where the time is discretized, $\partial\Psi/\partial t$ is replaced by $(\Psi^{new}-\Psi^{old})/\Delta t$ where Δt is the time division. If $H\Psi$ is replaced by $H\Psi^{old}$ as in the explicit scheme, Ψ^{new} can be expressed as:

$$\Psi^{new} = (1 + \Delta t/\hbar i\, H)\, \Psi^{old} \qquad \text{(A3)}$$

The wavefunction $\Psi(z,t)$ at any time can be evaluated by iterating equation (A3). However, the result from this explicit scheme is usually unstable

because the norm of the operator $1 + \Delta t/\hbar i\ H$ is typically larger than unity [1]. An alternative way, called Crank-Nicolson implicit scheme, is to replace $H\Psi$ by $(H\Psi^{new} + H\Psi^{old})/2$ instead of $H\Psi^{old}$ only. Using this replacement, we obtain:

$$\Psi^{new} = [\ (1 + \Delta t/2\hbar i\ H) / (1 - \Delta t/2\hbar i\ H)\ ]\ \Psi^{old} \qquad (A4)$$

Since the norm of $(1 + \Delta t/2\hbar i\ H) / (1 - \Delta t/2\hbar i\ H)$ is unity as H is hermitian, the result from this implicit scheme is relatively stable [1].

In practice, the operator $(1 + \Delta t/2\hbar i\ H) / (1 - \Delta t/2\hbar i\ H)$ is rewritten as $-1 + 2/(1 - \Delta t/2\hbar i\ H)$ in equation (A4). Since the operator H involves a second spatial derivative of $\Psi(z,t)$, equation (A4) consists of terms of three neighboring Ψ^{new}'s: $\Psi^{new}(z=z_o-\Delta z)$, $\Psi^{new}(z=z_o)$, $\Psi^{new}(z=z_o+\Delta z)$ in a discretized spatial region where the space division is Δz. In solving Ψ^{new} in equation (A4), the boundary conditions of Ψ^{new} has to be known [1].

A 2 Boundary Conditions

In the study of Tera Hertz DBRT, the double barrier structure is modulated in time as discussed in Chapter Three. Since the potential of the leftmost layer is static in time, the wavefunction at the left boundary is constant in time which is the sum of the incoming and reflected plane wave (neglect the trivial exponential factor $e^{-i\omega t}$) until the time-modulated reflection from the double barrier structure propagates to the left boundary. However, since the boundary is chosen to be far away from the double barrier structure, the modulated reflection does not have enough time to reach the boundary in the simulation. Therefore, we take the

wavefunction at the left boundary to be constant over time throughout the simulation.

The boundary condition for the wavefunction at the right boundary is different from constant. Since the potential of the rightmost layer is modulated in time, the wavefunction is changing even though the time-modulated transmitted wave outcoming from the double barrier structure has not yet reached the right boundary. The Schrödinger equation in this layer is:

$$\hbar\, i \frac{\partial \Psi}{\partial t} = - \frac{\hbar^2}{2m^*} \frac{\partial^2 \Psi}{\partial z^2} + e\, [\, - V_b + V_m \sin(\omega t)\,]\, \Psi \tag{A5}$$

whose solution is:

$$\Psi(z,t) = \Psi(z,0) \exp\left\{ - \frac{i}{\hbar} \int_0^t e\, V_m \sin(\omega t')\, dt' \right\} \tag{A6}$$

where $\Psi(z,0)$ is the transmitted plane wave and the factor $e^{-i\omega t}$ is dropped again. Hence, on the right boundary, the wavefunction is changing according to equation (A6) when the modulated transmitted wave from the double barrier has not reached the right boundary.

A 3 Reference

[1] Steve E. Koonin, Computational Physics, First Edition, page 161, Benjamin/Cummings, Menlo Park (1986).